Received March 31, 2020, accepted April 14, 2020, date of publication April 21, 2020, date of current version May 15, 2020.

Digital Object Identifier 10.1109/ACCESS.2020.2989370

A Highly Independent Multiband Bandpass Filter Using a Multi-Coupled Line Stub-SIR With Folding Structure

TEGUH FIRMANSYAH[1], (Member, IEEE), MUDRIK ALAYDRUS[2], (Senior Member, IEEE), YUYU WAHYU[3], (Member, IEEE), EKO TJIPTO RAHARDJO[1], (Member, IEEE), AND GUNAWAN WIBISONO[1], (Member, IEEE)

[1]Department of Electrical Engineering, Universitas Indonesia, Depok 16424, Indonesia
[2]Department of Electrical Engineering, Universitas Mercu Buana, Jakarta 11650, Indonesia
[3]Research Centre for Electronics and Telecommunications, Indonesian Institute of Sciences, Bandung 40135, Indonesia

Corresponding author: Gunawan Wibisono (gunawan@eng.ui.ac.id)

This work was supported by the QQ Project Grant (Universitas Indonesia) under Grant NKB-0299/UN2.R3.1/HKP.05.00/2019.

ABSTRACT The main problem in designing a multiband bandpass filter (BPF) is making each passband response highly independent, where each bandwidth of multiband BPF can be controlled and adjusted separately. To overcome this problem, this paper proposes a highly independent multiband BPF based on a multicoupled line stub-SIR with a folding structure. The proposed multiband BPF is constructed as a multicoupled line to generate a highly independent inter-passband. Moreover, the multiband performance is produced separately and independently by using three sets of resonators: resonator *A1/A2* (R_{A1} and R_{A2}), resonator *B1/B2* (R_{B1} and R_{B2}), and resonator *C1/C2* (R_{C1} and R_{C2}). The three passband frequencies can be independently arranged and designed. To miniaturize the multiband BPF, a folding structure is also proposed. As a result, the multiband BPF has a compact size that is reduced by over 61.29 % compared to previous structures. The even-odd excitation model and the equivalent circuit model are used to analyze the multiband BPF structure. This BPF is designed for GPS applications at 1.57 GHz, WCDMA (3G) at 1.8 GHz, WLAN (WiFi) at 2.4 GHz, LTE (4G) at 2.6 GHz, and 5G communication at 3.5 GHz. To evaluate and validate the proposed structure of the multiband BPF, the circuits are fabricated and tested. The simulated and measured results of the multiband BPF show good agreement. In conclusion, the proposed multiband BPF structure has a highly independent inter passband response and a compact size.

INDEX TERMS Compact, folding structure, highly independent, multiband BPF.

I. INTRODUCTION

In modern wireless communications, multiband bandpass filters (BPFs) are essential components in a variety of wireless technologies with simultaneous multistandard applications [1], [2], such as global positioning system (GPS), wireless local area network (WLAN/WiFi), global system for mobile communications (GSM/2G), wideband code division multiplexing access (WCDMA/3G), long term evolution (LTE/4G), [2], [3] and 5G communications [4]. As an important subsystem of multiband wireless transceivers, multiband BPFs with excellent performance and the capability to support wireless technology by concurrently reducing interference and noise at multiple frequencies are in high demand [5], [6].

The fundamental part of multiband BPF design lies in the resonator structure. Recently, researchers have explored a multiband BPF base on a crossed resonator [7]. In [7], the crossed resonator successfully produced multiresonant frequencies. Furthermore, to reduce the multiband BPF size, the assembled resonator was proposed by [8], and the meander coupled-line resonator was investigated by [9]. As a result, the size of multiband BPFs is more compact. However, each passband response is not independent. Furthermore, the lumped element structure was suggested by [10]. However, the addition of lumped elements makes the filter structure more complex. Other multiband BPFs have been generated from substrate integrated waveguide (SIW) resonators [11], [12] and high temperature superconducting

The associate editor coordinating the review of this manuscript and approving it for publication was Raghvendra Kumar Chaudhary.

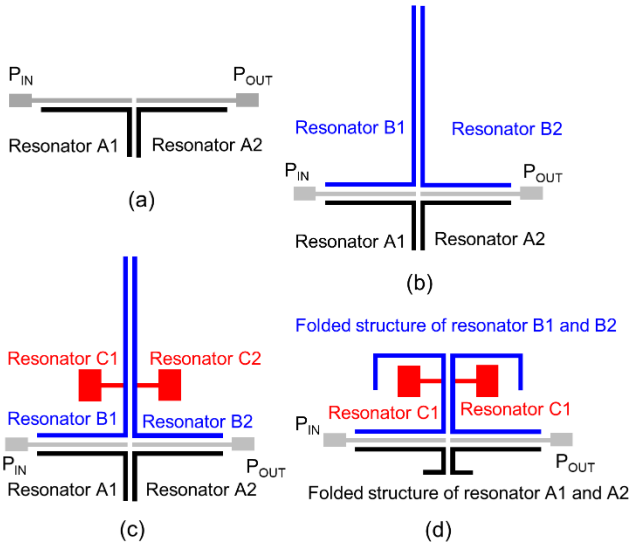

FIGURE 1. The proposed resonator structure for independent multiband BPF; (a) single-band BPF, (b) independent dual band BPF, (c) independent multiband BPF, and (d) miniaturized independent multiband BPF.

resonators [13]. However, for these methods, manufacturing is difficult, and the inter-passband have a low independence. The promising method of multiband BPFs is based on step impedance resonators (SIRs) such as the stub-loaded SIR [14], [15], quarter-wavelength SIR [16], asymmetric SIR [17], [18], coupled-line SIR [19], multimode SIR [20], and trisection SIR [21]. These resonators have achieved a good insertion loss $|S_{21}|$ and reflection coefficient $|S_{11}|$, and they have a low-isolation interband. However, these resonator structures have drawbacks such as a large size, complex structure, and non independent structure.

The dual-band independent BPFs was proposed by [22], and the short stub-loaded SIR and tri-section SIR resonator were used. However, these BPFs showed low independency at the upper bands and still worked at the dual passband. A tunable dual-band bandpass filter was proposed by [23], [24], but this BPF has drawbacks such as requiring active components and a power supply. A coplanar waveguide (CPW) bandpass was proposed by [25], but this BPF has a complex structure. An independent multiband BPF was proposed by [26]. To produce the multiband BPF, separated electric and magnetic coupling (SEMC) was proposed. However, this BPF has low independence at the first passband. Another independent multiband BPF was proposed by [27], but the insertion loss values are poor. The open-loop resonator was proposed by [28], but this filter also has low independence at the first passband. A dual composite right- and left-handed (D-CRLH) resonator was proposed by [29], but the resonator structure is quite complex, hard to extract, with non independent response.

This paper proposes a highly independent multiband bandpass filter using a multicoupled line stub-SIR with a folding structure, as shown in Fig 1(a) to 1(d). Fig 1(a), 1(b), 1(c), and 1(d) illustrate a single-band BPF, an independent dual-band BPF, an independent multiband BPF, and a miniaturized independent multiband BPF, respectively. The proposed multiband BPF is constructed with a multicoupled line to generate a highly independent inter passband. Moreover, the multiband performance is produced separately and independently by using three sets of resonators: resonator *A1/A2* (R_{A1} and R_{A2}), resonator *B1/B2* (R_{B1} and R_{B2}), and resonator *C1/C2* (R_{C1} and R_{C2}). Resonators A and B have an L-shaped structure. These resonators are placed at the upper and lower feeding lines, respectively. Furthermore, resonators *A* and *B* are designed for the first passband (f_{CA}) and the second passband (f_{CB}), respectively. The third resonator, resonator *C*, is a stub-step impedance resonator (SIR) embedded at the center of resonator B (R_{B1} and R_{B2}) to generate the third passband (f_{CC}), which can be clearly seen in Fig 1(c). Moreover, to miniaturize the multiband BPF, a folding structure is also proposed. This method can reduce the size of a multiband BPF by more than half, as shown in Fig 1(d). The three passband frequency responses can be tuned independently, as shown in Fig 2(a) to 2(c).

Here, high independence means that each passband response does not depend on another passband, so the filter response can be controlled and adjusted separately and individually. Fig 2(a) shows that the first passband (f_{CA}) can be varied by tuning the dimensions of resonator *A1/A2* (R_{A1} and R_{A2}). The f_{CB} and f_{CC} can be adjusted by varying the dimensions of resonator *B1/B2* (R_{B1} and R_{B2}) and resonator *C1/C2* (R_{C1} and R_{C2}), respectively.

The significant contributions of this paper are as follows.

1) Most previous studies have focused on multiband BPF design [8]–[30] without considering the independence of inter-passbands. As novelty, we focus on highly independent multiband BPF. This structure is making each passband response highly independent, where each band of multiband BPF can be controlled and adjusted separately.
2) The important feature of multicoupled line stub-SIR with a folding resonator structure is its highly independent performance with a simple structure and it can be easily analyzed and manufactured.
3) The three passband frequencies could be tuned independently and separately, as shown by the independent response of the insertion loss $|S_{21}|$ and the reflection coefficients $|S_{11}|$ at each passband and by the different direction of the surface current flows.
4) The folding structure method successfully reduces the multiband BPF dimensions by over 61.29 %, which makes the proposed multiband BPF very compact. The multiband BPF has a size of 0.32 $\lambda_G \times$ 0.31 λ_G. After the folding structure was applied, the multiband BPF size became 0.32 $\lambda_G \times$ 0.12 λ_G, where λ_G is the wavelength of the fundamental frequency
5) The proposed multiband BPF has performance advantages such as an excellent insertion loss $|S_{21}|$, a reflection coefficient $|S_{11}|$ with good transmission zeros and

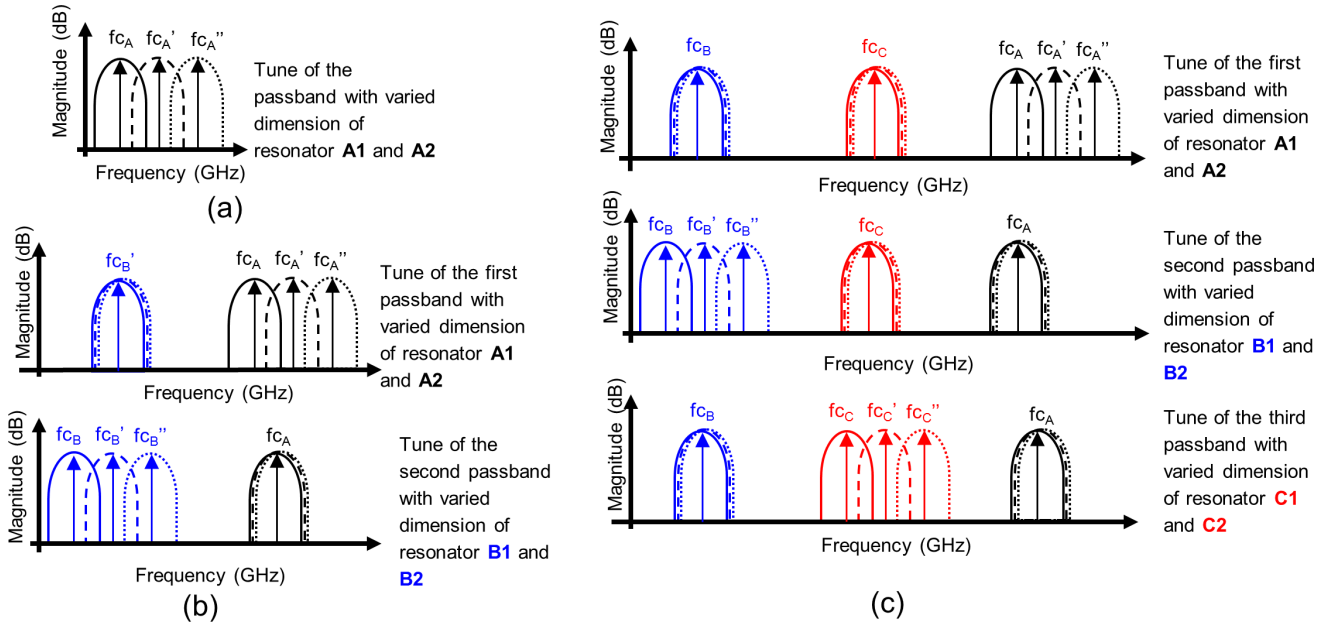

FIGURE 2. The independent filter response with varied resonator dimensions. (a) Single-band BPF response, (b) independent dual-band BPF response, and (c) independent multiband BPF response.

an isolation interband. The validity of the performance is shown by the excellent agreement between the simulated and measured results.

6) Finally, the proposed multiband BPF structure can be applied for 5G communication at 3.5 GHz.

To optimize the structure of the multiband BPF the Momentum Advance Design Systems (ADS) simulation was used.

Furthermore, the multiband BPF is fabricated on an RT/Duroid 5880 substrate with a permittivity of 2.2 and a thickness of 1.575 mm.

To validate the proposed method, the multiband BPF has been tested. The structure of this paper is as follows. The first section gives a brief overview of multiband BPF design and research. The second section describes and analyzes the structure of coupled-line resonators, single-band BPFs, independent dual-band BPFs, and independent multiband BPFs. The third section focuses on the implementation and validation of the resonator structure and its miniaturization strategy. Finally, section 4 concludes this research.

II. PROPOSED COUPLED-LINE RESONATOR STRUCTURE AND THE DESIGN OF SINGLE-BAND, DUAL- BAND, AND MULTIBAND BPFS

A. COUPLING STRUCTURE AND EXTERNAL QUALITY FACTOR

The proposed single coupled-line resonator structure is shown in Fig 3(a). The input-coupled line is directly connected to the 50-Ω port 1 (P_{IN}), and the other end of the resonator is connected to the 50-Ω port 2 output (P_{OUT}). This structure is used to investigate the external quality factor (Qe), coupling coefficient (M), and $|S_{21}|$ values under weak

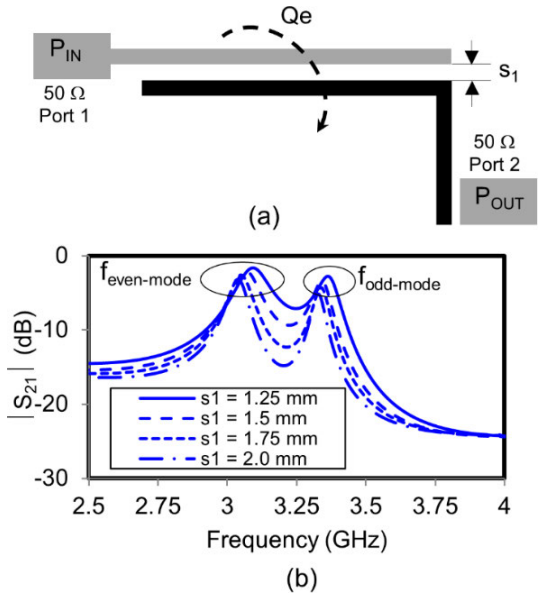

FIGURE 3. (a) The resonator structure for analysis of an external quality factor (Qext), (b) The simulated result of $|S_{21}|$ for the resonator structure under weak coupling with different s_1 values.

coupling with different gaps (s_1). Fig 3(b) shows the simulated results of odd-mode and even-mode frequency of $|S_{21}|$ with varied gaps (s_1). The resonant frequencies (f_C) value are determined by odd-mode resonant frequency ($f_{odd-mode}$) and even-mode resonant frequency ($f_{even-mode}$). Usually, the $f_{odd-mode}$ is higer than $f_{even-mode}$ and the resonant frequencies (f_C) is in the middle of the $f_{odd-mode}$ and $f_{even-mode}$. It can be seen that the $f_{odd-mode}$ and $f_{even-mode}$ excitations are shifted

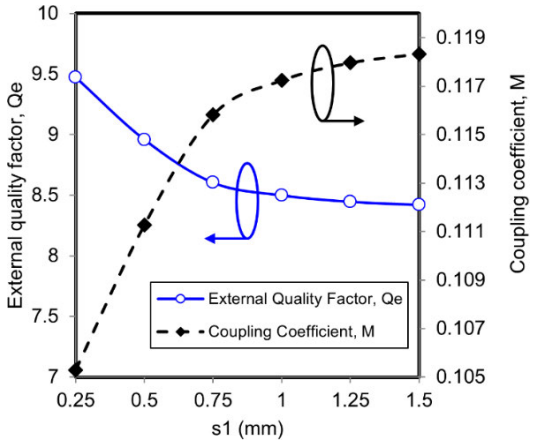

FIGURE 4. External quality factor (Qe) and coupling coefficient (M).

by different gap values (s_1). However, the resonant frequencies (f_C) remains stable, indicating that the gap variations do not affect the f_C values.

Furthermore, the coupling coefficient (M) and the external quality factor (Qe) should be determined. The coupling coefficient (M) of the resonator structure can be calculated by [31], [32]

$$M = \frac{f_o^2 - f_e^2}{f_o^2 + f_e^2} \tag{1}$$

where f_o and f_e are the odd-mode and even-mode frequency excitations, respectively. The simulation results of M under different gaps (s_1) is shown in Fig 4. Moreover, the external quality factor (Qe) can be calculated by [31], [32]

$$Qe = \frac{f_C}{BW} \tag{2}$$

where f_C and BW are the resonant frequency and the bandwidth, respectively.

B. DESIGN OF SINGLE-BAND BPF

The implementation of the coupled line as a single-band BPF is shown in Fig 5(a), and the coupling structure is shown in Fig 5(b). In the BPF topology, W_f, W_0, W_1, and W_2 represent the width of the resonator, and l_f, l_0, l_1, and l_2 represent the length of the resonator. Furthermore, the resonator structure consists of several transmission lines with different characteristic impedances Z_N (for $N = f, 0, 1, 2$) and corresponding electrical lengths θ_N (for $N = f, 0, 1, 2$).

The coupling structure for the single-band BPF with resonators R_{A1} and R_{A2} as the main resonator is illustrated in Fig 5(b). This BPF is symmetrical on the T-T' plane. M_{S1} and M_{2L} represent the external quality factor and the electric coupling of input-output port, respectively. Furthermore, M_{MN} are the coupling matrix value between two resonator as shown in Table 1. The value coupling matrix was obtained using optimization technique [12]. The nonlinear least-squares and the minimum-maximum algorithm were used.

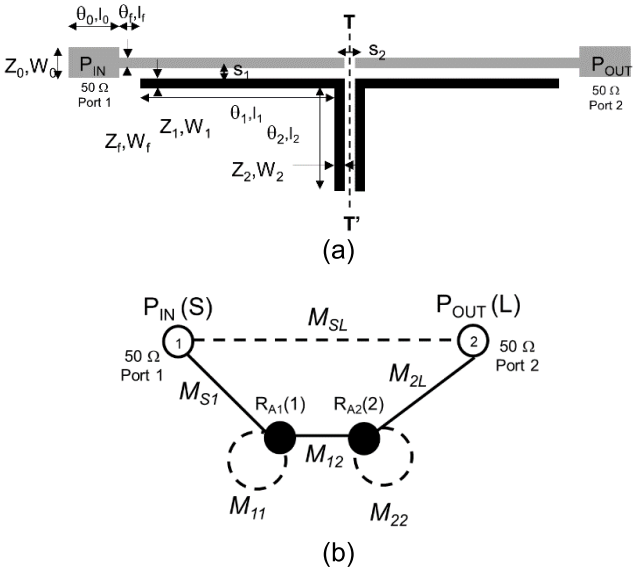

FIGURE 5. The proposed single-band BPF structure. (a) Filter topology, (b) Coupling structure.

TABLE 1. Coupling matrix of single-band BPF structure.

M_{MN}	$M = S$	$M = 1$	$M = 2$	$M = L$
$N = S$	0	0.5795	0	0.1535
$N = 1$	0.5795	0.1377	-0.5833	0
$N = 2$	0	-0.5833	0.1377	0.5795
$N = L$	0.1535	0	0.5795	0

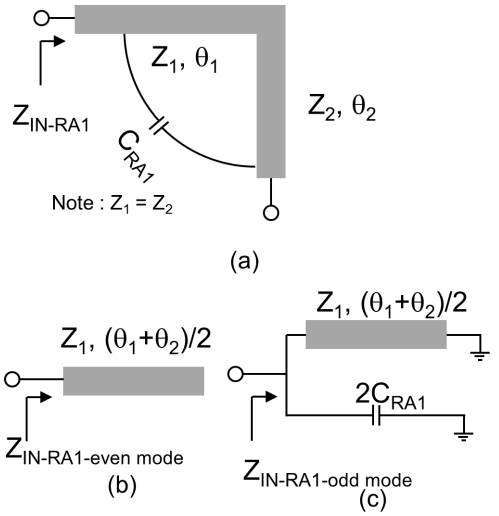

FIGURE 6. (a) The equivalent circuit model for resonator *A1*, (b) the equivalent circuit model for the even-mode of resonator *A1*, (c) the equivalent circuit model for the odd-mode resonator *A1*.

To investigate the BPF characteristics, the structure extractions should be provided as shown in Fig 6(a)-6(c). The equivalent circuit model for resonator *A1* (R_{A1}), the equivalent circuit model for the even-mode resonator, and the equivalent

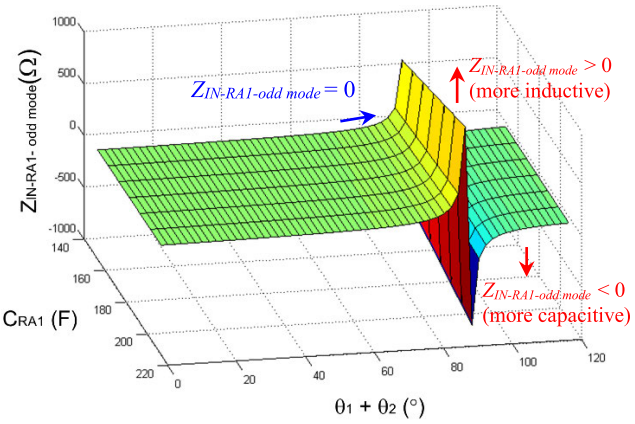

FIGURE 7. The variation of $Z_{IN-RA1\ odd-mode}$ versus $\theta_1 + \theta_2$ and C_{RA1}.

circuit model for the odd-mode resonator are shows in Fig 6(a), 6(b), and 6(c), respectively.

To simplify analysis and design, the values Z_1 and Z_2 are equal even if the length $\theta_1 \neq \theta_2$. Furthermore, because resonator R_{A1} has an L-shape structure, the electric coupling (E_1) based on the capacitive (C_{RA1}) factor should be included in the calculation of impedance [33]. Thus, to determine the resonant frequency, the full equivalent circuit model for resonator *A1* (R_{A1}) should be derived as shown in Fig 6(a).

The resonant frequencies for even-mode and odd-mode excitation can be determined from the impedance condition at $Z_{IN} = \infty$ or the admittance condition $Y_{IN} = 0$ [5], [6], [31]. Fig 6(b) shows the circuit model for the even-mode with the input impedance $Z_{IN-RA1-even\ mode}$, which has an open-circuit transmission line. Therefore, the $Z_{IN-RA1-even\ mode}$ can be determined as follows:

$$Z_{IN-RA1-even\ mode} = -jZ_1 \cot\left(\frac{\theta_1 + \theta_2}{2}\right) \tag{3}$$

Moreover, Fig 6(c) shows the equivalent circuit model for the odd-mode. Because $Z_{IN-RA1-odd\ mode}$ has a shut structure and is shunt to C_{RA1}, the $Z_{IN-RA1-odd}$ mode value can be calculated as

$$\frac{1}{Z_{IN-RA1-odd\ mode}} = \frac{1}{-jZ_1 \tan\left(\frac{\theta_1+\theta_2}{2}\right)} + j\omega 2_{CA} C_{RA1} \tag{4}$$

Furthermore, Eq (4) can be deduced as

$$Z_{IN-RA1-odd\ mode} = \frac{jZ_1 \tan\left(\frac{\theta_1+\theta_2}{2}\right)}{1 - 2Z_1\omega_{CA}C_{RA1} \tan\left(\frac{\theta_1+\theta_2}{2}\right)} \tag{5}$$

To meet the resonant conditions $Z_{IN} = \infty$ or $Y_{IN} = 0$, the denominator is set as follows [5], [6], [31]:

$$1 - 2Z_1\omega_{CA}C_{RA1} \tan\left(\frac{\theta_1 + \theta_2}{2}\right) = 0 \tag{6}$$

The resonant frequency can be calculated as follows:

$$\omega_{CA} = \frac{1}{2Z_1 C_{RA1} \tan\left(\frac{\theta_1+\theta_2}{2}\right)} \tag{7}$$

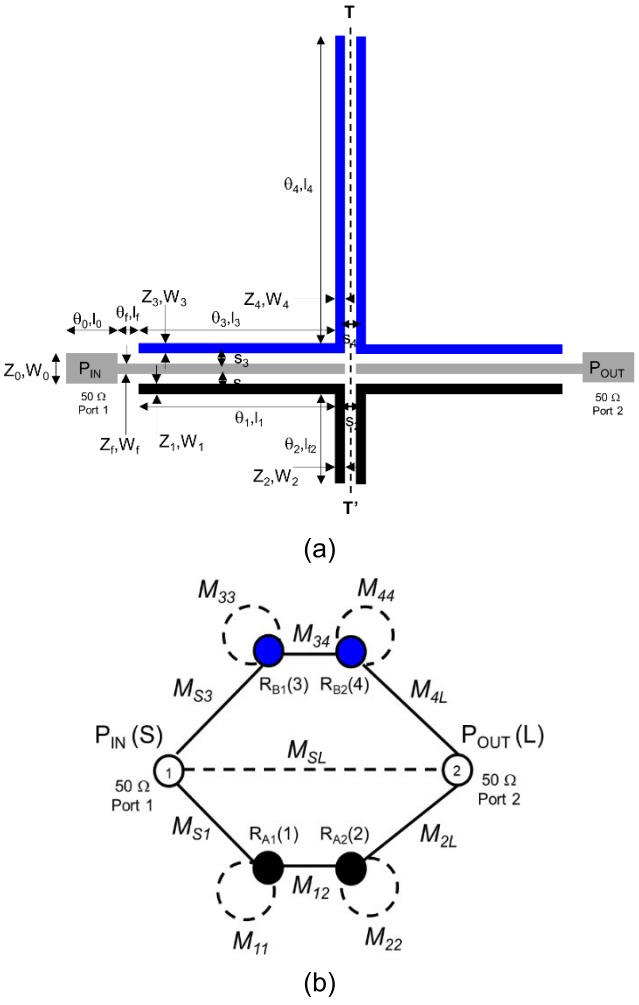

FIGURE 8. The proposed independent dual-band BPF structure (a) Filter topology, (b) Coupling structure.

or the value of f_{CA} can be determined as

$$f_{CA} = \frac{1}{\pi 4Z_1 C_{RA1} \tan\left(\frac{\theta_1+\theta_2}{2}\right)} \tag{8}$$

where Z_1 is the characteristic impedance, C_{RA1} is the capacitance, $\theta_1 + \theta_2$ are the electrical lengths, and $Z_1 = Z_2$. The variation of $Z_{IN-RA1-odd\ mode}$ versus $(\theta_1 + \theta_2)$ and C_{RA1} is shown in Fig 7.

The effect of $\theta_1 + \theta_2$ and C_{RA1} to $Z_{IN-RA1-odd\ mode}$ is shown in Fig 7. We can see that C_{RA1} has a lower impact on the impedance value of $Z_{IN-RA1-odd\ mode}$. However, the value of $Z_{IN-RA1-odd\ mode}$ has largely determined by the length of $\theta_1 + \theta_2$. For the value of $\theta_1 + \theta_2$ lower than 80° and upper than 90°, $Z_{IN-RA1-odd\ mode}$ is more capacitive. Moreover, we can see that the value of $\theta_1 + \theta_2$ between 80° and 90°, making $Z_{IN-RA1-odd\ mode}$ more inductive. Furthermore, the resonance occurs when the imaginary part of the $Z_{IN-RA1-odd\ mode}$ is zero.

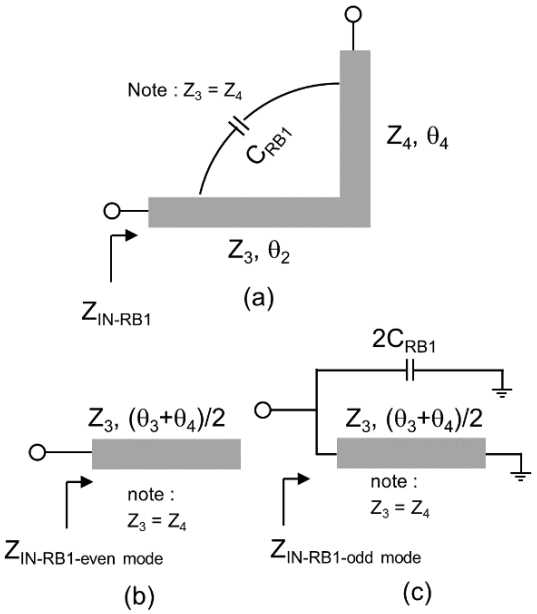

FIGURE 9. (a) Equivalent circuit model for resonator *B*1, (a) Equivalent circuit model for the even-mode resonator *B*1, (b) Equivalent circuit model for the odd-mode resonator *B*1.

C. DESIGN OF DUAL-BAND BPF

The second section is focused on the dual-band BPF. The dual-band BPF response is obtained by adding the resonator *B1/B2* (R_{B1} and R_{B2}) as shown in Fig 8(a). The resonator *B1/B2* (R_{B1} and R_{B2}) is placed at the upper side of the feeding line. R_{B1} and R_{B2} are L-shaped and have a back-to-back coupled structure. Consequently, the network coupling structure is magnetic coupling (M_2) [40]. The detailed structure of the proposed dual-band BPF is shown in Fig 8(a), and the BPF is symmetrical on the T-T' plane. In the dual-band BPF topology, W_0, W_f, W_1, W_2, W_3, and W_4 represent the width of the resonator and correspond to the characteristic impedances Z_N (for $N = f, 0, 1, 2, 3, 4$). Furthermore, the l_0, l_f, l_1, l_2, l_3, and l_4, values represent the length of the resonator, with corresponding electrical lengths θ_N (for $N = f, 0, 1, 2, 3, 4$).

As shown in Fig 8(b), the coupling structure of the dual-band BPF is expanded from the coupling structure of the single-band BPF in Fig 5(b). It can be seen that the additional coupling at the upper feeding line will change the coupling structure there. The complete coupling matrix of dual-band BPF structure is shown in Table 2.

The terminal 50-Ω port is connected to P_{IN} and P_{OUT} as the input-output port. To evaluate the resonant frequency (f_{CB}), the equivalent circuit model for resonator *B1* (R_{B1}), as shown in Fig 9(a), should be provided. To simplify analysis and design, the values Z_3 and Z_4 are equal, but $\theta_1 \neq \theta_2$. Because resonator R_{B1} is L-shaped, the capacitance (C_{RB1}) value should be included in calculations [33]. The value coupling matrix was obtained using optimization technique [12]. The nonlinear least-squares and the minimum-maximum algorithm were used.

TABLE 2. Coupling matrix of dual-band BPF structure.

M_{MN}	$M = S$	$M = 1$	$M = 2$	$M = 3$	$M = 4$	$M = L$
$N = S$	0	0.299	0	-0.264	0	0.103
$N = 1$	0.299	0.380	0.707	0	0	0
$N = 2$	0	0.707	-1.030	0	0	0.932
$N = 3$	-0.264	0	0	-26.271	-51.382	0
$N = 4$	0	0	0	-51.382	-103.010	-0.699
$N = L$	0.103	0	0.932	0	-0.699	0

Fig 9(a), 9(b), and 9(c) show the equivalent circuit models for R_{B1}, the even-mode resonator R_{B1}, and the odd-mode resonator R_{B1}, respectively. $Z_{IN-RB1-even\ mode}$ can be determined as follows:

$$Z_{IN-RB1-even\ mode} = -jZ_3 \cot\left(\frac{\theta_3 + \theta_4}{2}\right) \tag{9}$$

Moreover, the $Z_{IN-RB1-odd\ \mathrm{mode}}$ has a shunt structure, so it can be calculated as

$$\frac{1}{Z_{IN-RB1-odd\ mode}} = \frac{1}{-jZ_3 \tan\left(\frac{\theta_3+\theta_4}{2}\right)} + j2\omega_{CB}C_{RB1} \tag{10}$$

Furthermore, Eq (10) can be deduced as

$$Z_{IN-RA1-odd\ mode} = \frac{jZ_3 \tan\left(\frac{\theta_3+\theta_4}{2}\right)}{1 - 2Z_3\omega_{CB}C_{RB1} \tan\left(\frac{\theta_3+\theta_4}{2}\right)} \tag{11}$$

To meet the resonant condition $Z_{IN} = \infty$ or $Y_{IN} = 0$, the denominator is set as follows:

$$1 - 2Z_3\omega_{CB}C_{RB1} \tan\left(\frac{\theta_3 + \theta_4}{2}\right) = 0 \tag{12}$$

The resonant frequency can be calculated as follows:

$$\omega_{CB} = \frac{1}{2Z_3C_{RB1} \tan\left(\frac{\theta_3+\theta_4}{2}\right)} \tag{13}$$

or the value of f_{CB} can be determined as

$$f_{CB} = \frac{1}{\pi 4Z_3C_{RB1} \tan\left(\frac{\theta_3+\theta_4}{2}\right)} \tag{14}$$

where Z_3 is the characteristic impedance, C_{RB1} is the capacitance, θ_2 and θ_3 are the electrical lengths, and $Z_3 = Z_4$.

D. DESIGN OF MULTIBAND BPF

The design of a highly independent multiband BPF and its miniaturization strategy are investigated in this section. Fig 10 (a) and 10 (b) show the proposed filter topology of an independent multiband BPF structure and the coupling structure, respectively. Furthermore, Table 3 shows the coupling matrix of multi-band BPF structure. The value coupling matrix was obtained using optimization technique [12]. The nonlinear least-squares and the minimum-maximum algorithm were used.

To produce the third passband (f_{CC}), the additional stub-stepped impedance resonators (Stub-SIR), namely, resonator

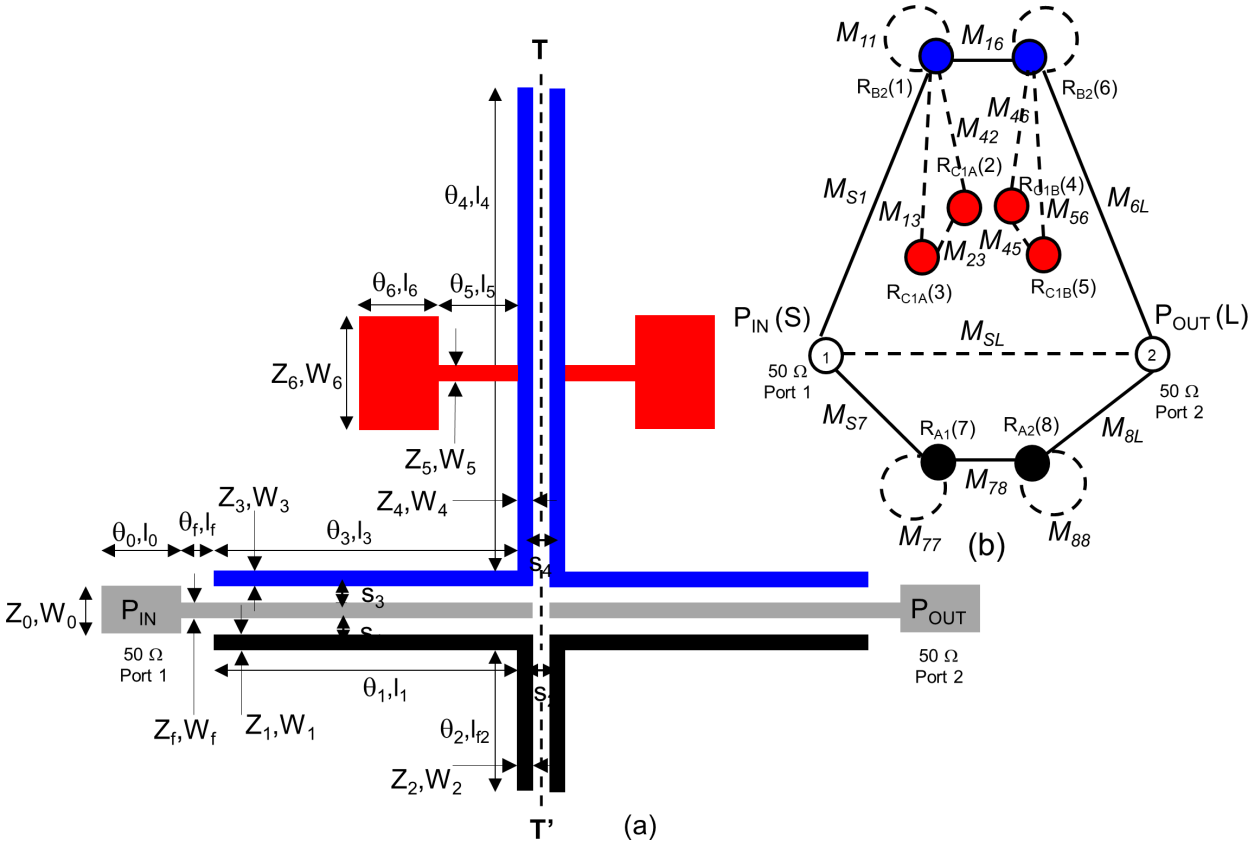

FIGURE 10. The proposed independent multiband BPF structure (a) Filter topology (b) Coupling structure.

C1/C2 (R_{C1} and R_{C2}), are embedded in resonator B (R_{B1} and R_{B2}), as shown in Fig 10(a). Resonator *C1/C2* has the SIR structure composed of two transmission lines such as (W_5, l_5, Z_5, θ_5) and (W_6, l_6, Z_6, θ_6). In the multiband BPF topology, W_f, W_0, W_1, W_2, W_3, W_4, W_5, and W_6 represent the width of the resonator and correspond to the characteristic impedances Z_N (for $N = f, 0, 1, 2, 3, 4, 5, 6$). Furthermore, l_f, l_0, l_1, l_2, l_3, l_4, l_5, and l_6, represent the length of the resonator with corresponding electrical lengths θ_N (for $N = f, 0, 1, 2, 3, 4, 5, 6$).

The multiband BPF coupling structure is shown in Fig 10(b). It can be seen that the additional Stub-SIR has changed the coupling structure at the upper resonator (R_{B1} and R_{B2}). Furthermore, the structured resonators are illustrated as R_{An}(for $n = 1, 2$), R_{Bn}(for $n = 1, 2$), and R_{Cn}(for $n = 1, 2$) for resonator *A1/A2*, resonator *B1/B2*, and resonator *C1/C2*, respectively.

To evaluate the resonant frequency, the equivalent circuit models for resonators *B1* and *C1* (R_{B1} and R_{C1}) should be investigated. They are shown in Fig 11(a). Fig 11(a), 11(b) and 11(c) show the equivalent circuit models for resonators *B1* and *C1* (R_{B1} and R_{C1}), the even-mode resonator (R_{B1} and R_{C1}), and the odd-mode resonator (R_{B1} and R_{C1}), respectively. The even-mode and odd-mode resonant frequencies can be determined from the impedance condition $Z_{IN} = \infty$ or the admittance condition $Y_{IN} = 0$ [5], [6], [31].

First, Z_{IN6} can be calculated as follows:

$$Z_{IN6} = -j2Z_6 \cot\theta_6 \tag{15}$$

Z_{IN5} can be determined as follows:

$$Z_{IN5} = \frac{jZ_5^2 \tan\theta_5 - j2Z_5Z_6 \cot\theta_6}{Z_5 + 2Z_6 \tan\theta_5 \cot\theta_6} \tag{16}$$

Then, the impedance $Z_{IN-RB1-RC1-even\ mode}$ can be determined as follows:

To meet the resonant condition $Z_{IN} = \infty$ or $Y_{IN} = 0$, the denominator (17), as shown at the bottom of the next page, is calculated as follows [5], [6], [31]:

$$2Z_3Z_5 + 2Z_3Z_6 \tan\theta_5 \cot\theta_6 - 4Z_5^2 \tan\theta_3 \times \tan\theta_5 + 2Z_5Z_6 \tan\theta_3 \cot\theta_6 = 0 \tag{18}$$

$$\frac{2Z_3}{Z_5} + \frac{2Z_3Z_6}{Z_5^2} \tan\theta_5 \cot\theta_6 - 4\tan\theta_3 \times \tan\theta_5 + \frac{4Z_6}{Z_5} \tan\theta_3 \cot\theta_6 = 0 \tag{19}$$

Eq(19) can be simplify as follows:

$$2K_1 + 2K_1K_2 \tan\theta_5 \cot\theta_6 - 4\tan\theta_3 \times \tan\theta_5 + 4K_2 \tan\theta_3 \cot\theta_6 = 0 \tag{20}$$

$$K_1 (2 + 2K_2 \tan\theta_5 \cot\theta_6) - 4\tan\theta_3 (\tan\theta_3 + K_2 \cot\theta_6) = 0 \tag{21}$$

TABLE 3. Coupling matrix of multi-band BPF structure.

M_{MN}	$M=S$	$M=1$	$M=2$	$M=3$	$M=4$	$M=5$	$M=6$	$M=7$	$M=8$	$M=L$
$N=S$	0	6.058	0	0	0	0	0	0.906	0	5.547
$N=1$	6.058	83.428	61.748	70.393	0	0	-2.073	0	0	0
$N=2$	0	61.748	0	103.026	0	0	0	0	0	0
$N=3$	0	70.393	103.026	0	0	0	0	0	0	0
$N=4$	0	0	0	0	0	-7.265	0.047	0	0	0
$N=5$	0	0	0	0	-7.265	0	1.788	0	0	0
$N=6$	0	-2.073	0	0	0.047	1.1788	0.0714	0	0	-2.004
$N=7$	0.906	0	0	0	0	0	0	0.001	0.207	0
$N=8$	0	0	0	0	0	0	0	0.207	0.001	-0.369
$N=L$	5.547	0	0	0	0	0	-2.004	0	-0.369	0

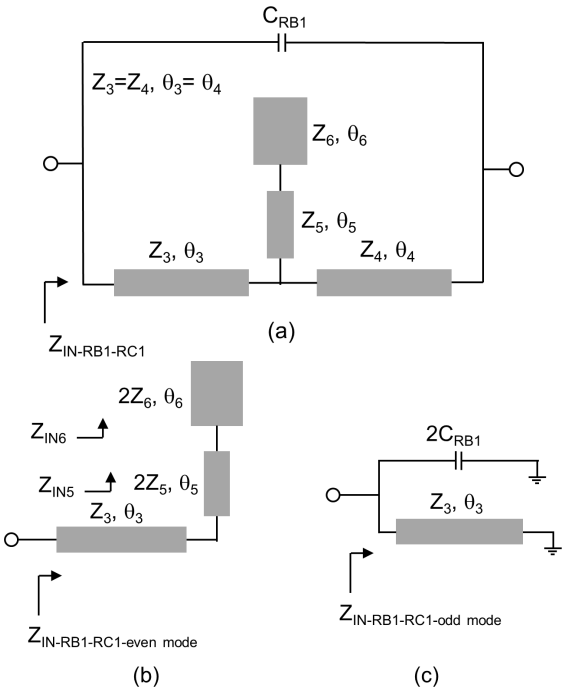

FIGURE 11. (a) Equivalent circuit model for upper resonator (*B*1 and *C*1), (b) Equivalent circuit model of upper resonator (*B*1 and *C*1) for the even-mode, (c) Equivalent circuit model of upper resonator (*B*1 and *C*1) for the odd-mode.

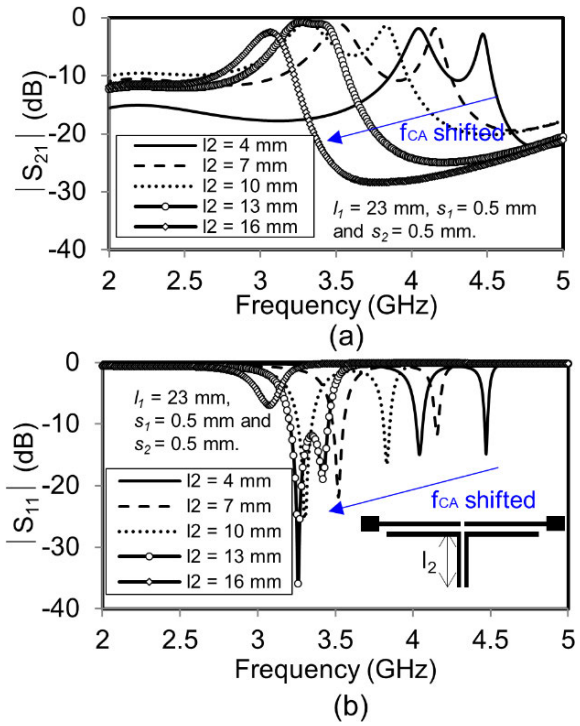

FIGURE 12. Simulation results of $|S_{21}|$ characteristics for varied lengths l_2, (b) $|S_{11}|$ characteristics for varied lengths l_2.

where

$$K_1 = \frac{Z_3}{Z_5} \tag{22}$$

$$K_2 = \frac{Z_6}{Z_5} \tag{23}$$

Moreover, $Z_{IN-RB1-RC1-odd\ mode}$ has a shunt structure as shown in Fig 11(c), so it can be calculated as

$$\frac{1}{Z_{IN-RB1-RC1-odd\ mode}} = \frac{1}{-jZ_3 \tan\theta_3} + j2\omega_3 C_{RB1} \tag{24}$$

Furthermore, Eq (27) can be deduced as

$$Z_{IN-RB1-RC1-odd\ mode} = \frac{jZ_3 \tan\theta_3}{1 - 2Z_3\omega_3 C_{RB1} \tan\theta_3} \tag{25}$$

To meet the resonant condition $Z_{IN} = \infty$ or $Y_{IN} = 0$, the denominator is set as follows [5], [6], [31]:

$$1 - 2Z_3\omega_3 C_{RB1} \tan\theta_3 = 0 \tag{26}$$

where Z_N (for $N = 3, 5, 6$) and θ_N (for $N = 3, 5, 6$) are the characteristic and electrical lengths, respectively.

$$Z_{IN-RB1-RC1-evenmode} = \frac{j4Z_3Z_5^2 \tan\theta_5 - j4Z_3Z_5Z_6 \cot\theta_6 + j2Z_3^2Z_5 \tan\theta_3 + j4Z_3^2Z_6 \tan\theta_3 \tan\theta_5 \cot\theta_6}{2Z_3Z_5 + 2Z_3Z_6 \tan\theta_5 \cot\theta_6 - 4Z_5^2 \tan\theta_3 \tan\theta_5 + 4Z_5Z_6 \tan\theta_3 \cot\theta_6} \tag{17}$$

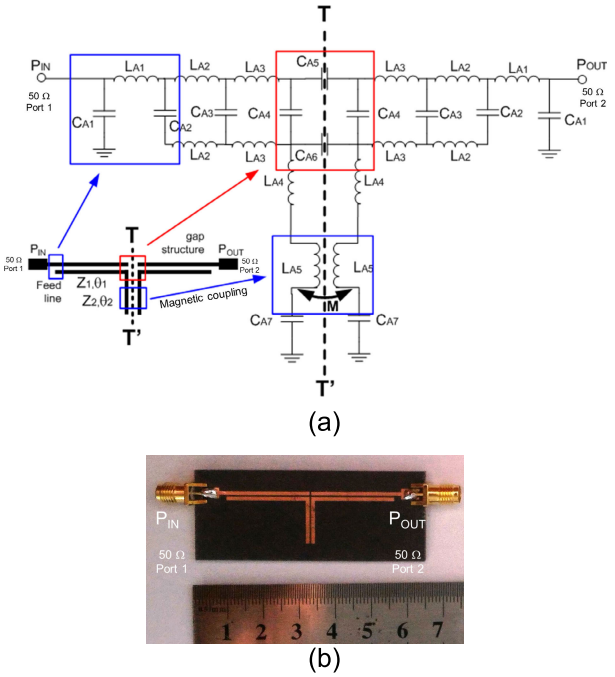

FIGURE 13. (a) The equivalent circuit model of the independent single-band BPF, (b) the photograph of the fabricated single-band BPF.

III. IMPLEMENTATION OF HIGHLY INDEPENDENT SINGLE-BAND, DUAL- BAND, AND MULTIBAND BPFS

A. IMPLEMENTATION OF SINGLE-BAND BPF STRUCTURE

The parametric simulation results are provided in Fig 12(a) and 12(b), which show the $|S_{21}|$ characteristics with varied lengths (l_2) and the $|S_{11}|$ characteristics with varied lengths (l_2), respectively. It is clearly seen from Fig 12(a) that the frequency center can be adjusted by varying the length (l_2). This figure also shows that the optimum value of $l_2 = 13$ mm. Moreover, the magnitude of $|S_{11}|$ must be set to lower than -10 dB to make sure that the reflection coefficient is low. These simulation results show that the value of the length l_2 corresponds with θ_2 and has a positive contribution to f_{CA}. This interesting finding confirms the usefulness of Eq (8) and shows that f_{CA} is affected by θ_2 when θ_1 is set to a constant value.

Fig 13 (a) and 13 (b) show the equivalent circuit model of a highly independent single-band BPF and a photograph of a fabricated single-band BPF, respectively. The equivalent circuit model of the single-band BPF is symmetrical on the T-T' plane.

The resonator structure consists of several passive components such as capacitor C_{An} (for $n = 1, 2, 3, 4, 5, 6, 7$) and inductor L_{An} (for $n = 1, 2, 3, 4, 5$). Because resonators R_{A1} and R_{A2} are L-shaped and the back-to-back structure is coupled, the coupled network is a magnetic coupling structure (M_1) [33]. The corner part of the resonator becomes more capacitive and is thus replaced as a capacitor. Fig 13(a) shows the detailed equivalent circuit.

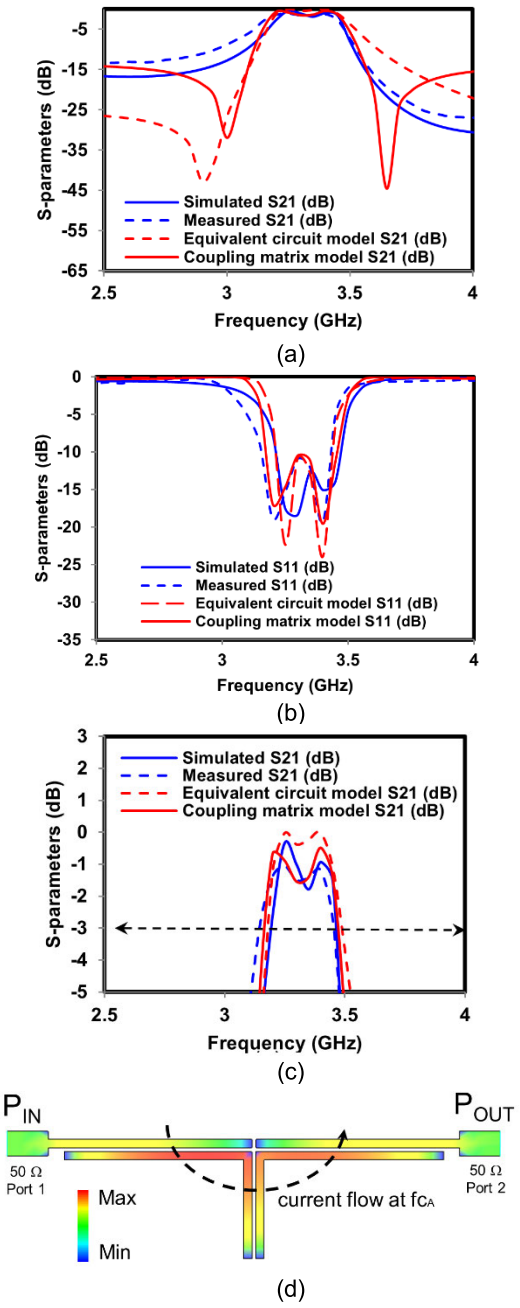

FIGURE 14. Simulated, measured, and equivalent circuit model results (a) $|S_{21}|$, (b) $|S_{11}|$, (c) bandwidth at $|S_{21}|$ at -3 dB, and (d) surface current flow at f_{CA}.

The simulation and optimization results are obtained with the ADS software. The overall dimensions of the single-band BPF are $W_0 = 3$ mm, $W_f = 1$ mm, $W_1 = 1$ mm, $W_2 = 1$ mm, $l_0 = 5$ mm, $l_f = 2$ mm, $l_1 = 23$ mm, $l_2 = 13$ mm, $s_1 = 0.5$ mm and $s_2 = 0.5$ mm. Furthermore, the values of the equivalent circuit models are $C_{A1} = 15$ pF, $C_{A2} = 1.5$ μ F, $C_{A3} = 15$ pF, $C_{A4} = 0.1$ pF, $C_{A5} = 150$ pF, $C_{A6} = 75$ pF, $C_{A7} = 75$ pF, $L_{A1} = 0.01$ pH, $L_{A2} = 300$ pH, $L_{A3} = 0.01$ pH, $L_{A4} = 89$ pH, and $L_{A5} = 14$ pH. The single-band BPF is fabricated on an RT/Duroid 5880 substrate and

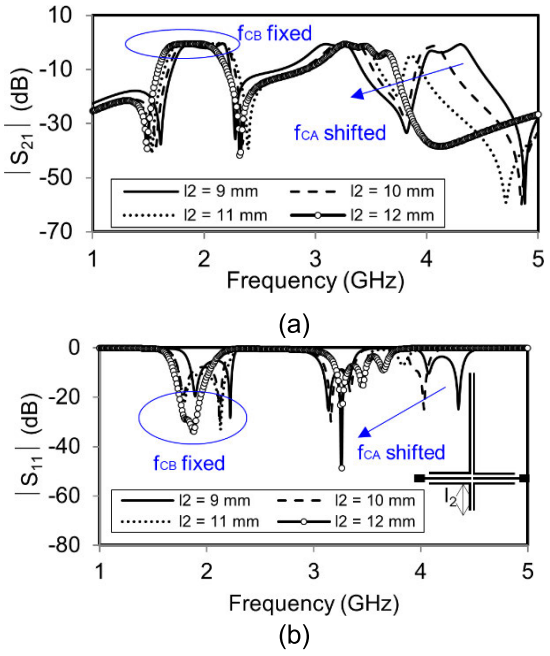

FIGURE 15. Simulation results of (a) $|S_{21}|$ characteristics with varied length l_2, (b) $|S_{11}|$ characteristics with varied length l_2.

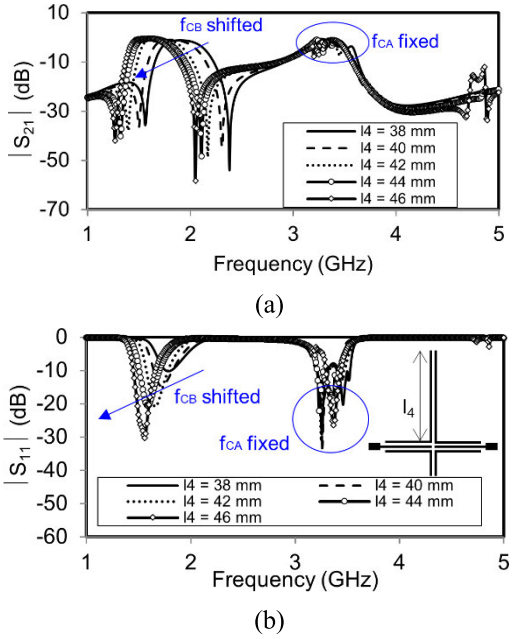

FIGURE 16. Simulation results of (a) $|S_{21}|$ characteristics with varied length l_4, (b) $|S_{11}|$ characteristics with varied length l_4.

is soldered to a 50-Ω input/output port, as shown in Fig 13(b). To evaluate the performance, the device under test (DUT) should be connected to a vector network analyzer (VNA). The R& S ZNB VNA was used to measure the BPF. Fig 14(a), 14(b), and 14(c) show the simulated, measured, equivalent circuit model, and coupling matrix model results of $|S_{21}|$ and $|S_{11}|$, with a bandwidth at $|S_{21}|$ of −3 dB. Fig 14(d) shows the surface current flow at f_{CA}.

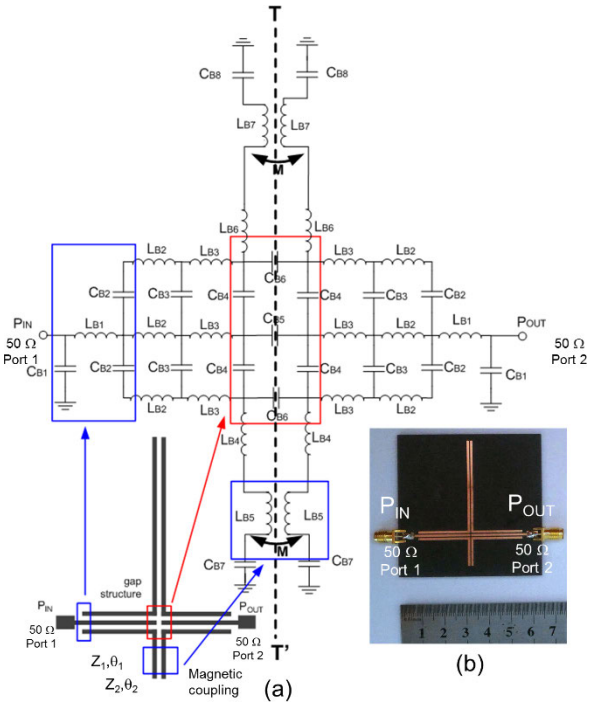

FIGURE 17. (a) The equivalent circuit model of the independent dual-band BPF, (b) photograph of the fabricated dual-band BPF.

TABLE 4. Dimensions of the dual-band BPF and values of the equivalent circuit model.

N	W_N *(mm)*	l_N *(mm)*	s_N *(mm)*
f	*1*	*2*	-
0	*3*	*5*	-
1	*1*	*23*	*0.5*
2	*1*	*13*	*0.5*
3	*1*	*23*	-
4	*1*	*44*	-

N	C_{BN} *(pF)*	L_{BN} *(pH)*
1	*15*	*0.01*
2	*165*	*135*
3	*2*	*330*
4	*120*	*420*
5	*5*	*105*
6	*195*	*3600*
7	*250*	*13*

TABLE 5. Comparison of dual-band BPF results.

Parameters	f_{CB}		f_{CA}	
	Sim	*Meas*	*Sim*	*Meas*
f_C *(GHz)*	1.75	1.75	3.45	3.45
FBW (%)	17.11	16.90	12.31	11.83
$\|S_{21}\|$ dB	-0.16	-0.41	-0.54	-1.14
$\|S_{11}\|$ dB	-14.37	-16.56	-22.38	-18.04
Trans. zeros	-47.70 dB at 2.25 GHz (sim)			
(Isolation interband)	-30.81 dB at 2.25 GHz (meas)			

*note: in our design f_{CA} is higher than f_{CB}

The simulated/measured results of the single-band BPF are 3.25 GHz/3.27 GHz, 8.09 %/9.14 %, −0.35 dB/−0.8 dB, −17.0 dB/−19.6 dB for the f_{CA}, fractional bandwidth (FBW), $|S_{21}|$, and $|S_{11}|$, respectively. The single-band BPF

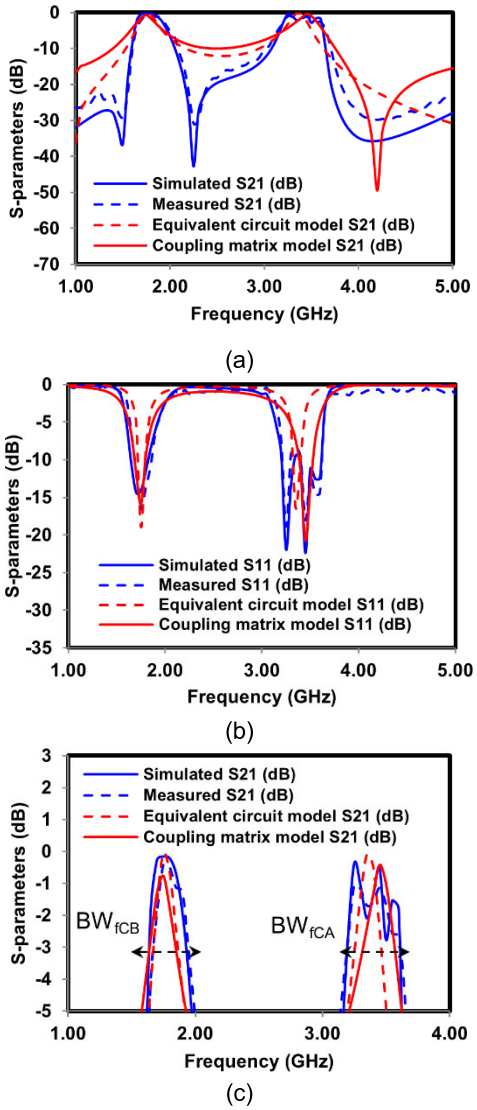

FIGURE 18. Simulated, measured, and equivalent circuit model results (a) $|S_{21}|$, (b) $|S_{11}|$, (c) bandwidth f_{CB} and f_{CA} at $|S_{21}| = -3$ dB.

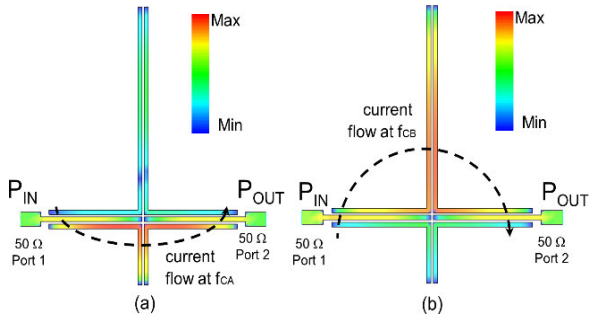

FIGURE 19. Surface current flow at (a) f_{CA}, (b) f_{CB}.

design strategies are validated by very good agreement between the measured and simulated results.

B. IMPLEMENTATION OF INDEPENDENT DUAL-BAND BPF STRUCTURE

This section discusses the optimization and implementation of an independent dual-band BPF. The dual-band BPF results

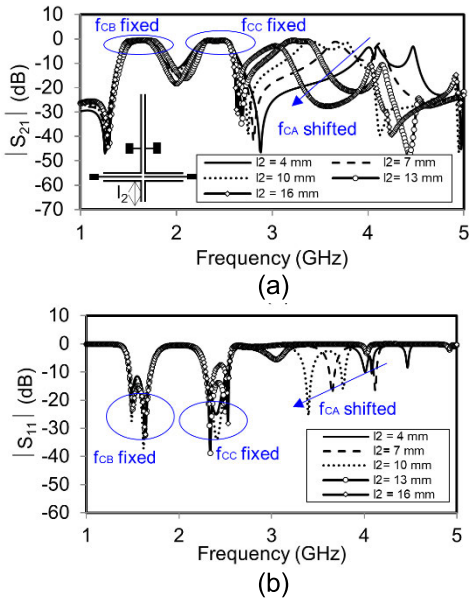

FIGURE 20. Simulation results of (a) $|S_{21}|$ characteristics with varied length l_2 and (b) $|S_{11}|$ characteristics with varied length l_2.

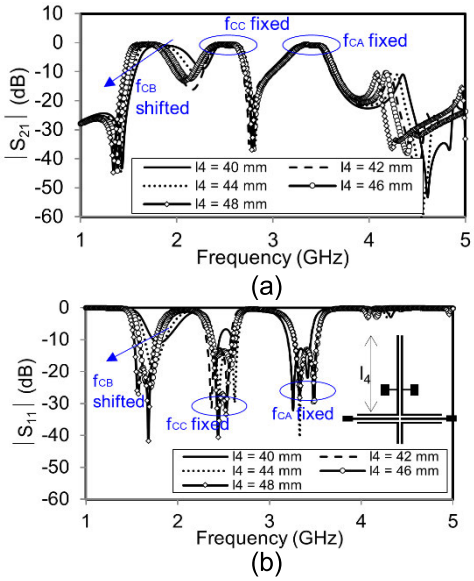

FIGURE 21. Simulation results of (a) $|S_{21}|$ characteristics with varied length l_4 and (b) $|S_{11}|$ characteristics with varied length l_4.

are provided in Fig 15(a) and 15(b), which show the magnitude of the $|S_{21}|$ characteristics with varied lengths (l_2) and the $|S_{11}|$ characteristics with varied lengths (l_2), respectively. Fig 15(a) shows that varying the value of length (l_2) can tune the $|S_{21}|$ passband of f_{CA} while the frequency f_{CB} remains constant/fixed. This result indicates that the proposed dual-band BPF has highly independent responses and illustrates that the insertion loss value of the passband is higher than -3 dB.

Fig 15(b) clearly shows that varying the length (l_2) can tune the value $|S_{11}|$ at passbands of frequency f_{CA}, whereas

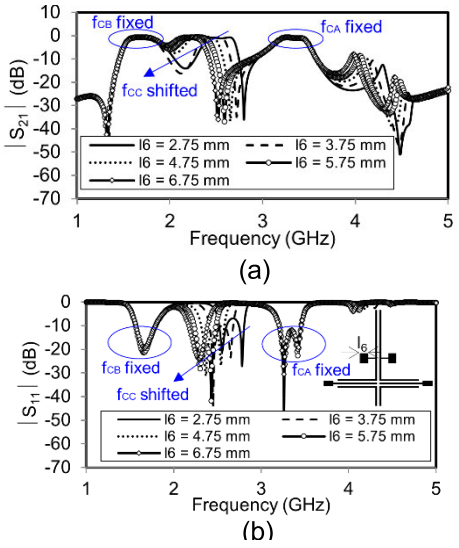

FIGURE 22. Simulation results of (a) $|S_{21}|$ characteristics with varied length l_6 and (b) $|S_{11}|$ characteristics with varied length l_6.

this change has only a slight influence on the passband f_{CB}. It is also observed that the value $|S_{11}|$ is better than -10 dB, which indicates that the dual-band BPF has a low reflection coefficient. Therefore, we can adjust the length of l_2 to tune the f_{CA} passband. Increasing l_2 will make the f_{CA} shift to a lower frequency, while decreasing l_2 will make the f_{CA} shift to a higher frequency.

Fig 16(a) and 16(b) illustrate the magnitude of the $|S_{21}|$ characteristics for varying lengths (l_4) and the $|S_{11}|$ characteristics for varying lengths (l_4), respectively. It is clearly seen that by varying the length (l_4), the frequency of f_{CB} will shift independently. However, f_{CA} will be stable. It is also shown that the values of $|S_{11}|$ and $|S_{21}|$ can be optimized to better than -10 dB and -3 dB, respectively. The passband f_{CB} can be controlled by the length (l_4). This finding confirms the usefulness of Eq (14) and shows that f_{CB} is affected by θ_4 when θ_3 is set as a constant value, with θ_4 corresponding to l_4. Therefore, this result shows that the two passband frequencies could be tuned independently and separately and demonstrates the successful design of a highly independent dual-band BPF.

Fig 17(a) and 17(b) show the equivalent circuit model of the independent dual-band BPF and a photograph of the fabricated dual-band BPF, respectively. The value of the magnetic coupling of the structures is indicated by M and is shown at the upper and lower resonators. The dimensions of the dual-band BPF and the values of the equivalent circuit model after optimization using the ADS software are shown in Table 4.

As shown in Fig 17(a), the equivalent circuit model consists of upper and lower feeding lines. Due to the high magnetic field, the coupling inter resonator is drawn as magnetic coupling. However, the equivalent circuit model at the center of the dual-band BPF is shown to be a capacitive circuit. Moreover, the photograph of the fabricated dual-band BPF

TABLE 6. Dimensions of the multiband BPF and values of the equivalent circuit model.

N	W_N (mm)	l_N (mm)	s_N (mm)
f	1	2	-
0	3	5	-
1	1	23	0.5
2	1	13	0.5
3	1	23	0.5
4	1	44	0.5
5	1	5	-
6	7	4.75	-

N	C_{CN} (pF)	L_{CN} (pH)
1	15	5
2	265	135
3	1	360
4	450	60
5	0.1	105
6	16	300
7	225	0.01
8	120	45
9	60	-
10	0.1	-

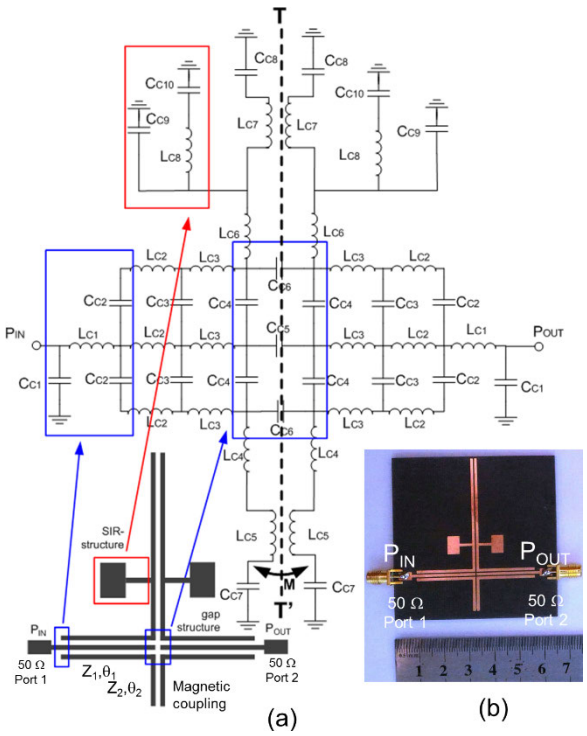

FIGURE 23. (a) The equivalent circuit model of the independent multiband BPF, (b) photograph of the fabricated multiband BPF.

shown in Fig 17(b) illustrates the complete dual-band BPF with 50-Ω port termination.

To verify the proposed BPF design, the fabricated results of the dual-band BPF must be tested. Fig 18 (a), 18(b), and 18(c) show the simulated, measured, equivalent circuit model, and coupling matrix model results of $|S_{21}|$, $|S_{11}|$, $|S_{21}|$ for a bandwidth f_{CB} and f_{CA} of -3 dB, respectively.

The results of simulated and measured dual-band BPFs are shown in Table 5.

Fig 19 (a) and 19(b) show the surface current flow at passband f_{CA} and passband f_{CB}, respectively. The surface current distribution at the f_{CA} band has flowed at the lower part of the feeding structure or it has flowed at the lower resonator. However, the surface current distribution at the f_{CB} band has flowed at the upper resonator. These results indicate

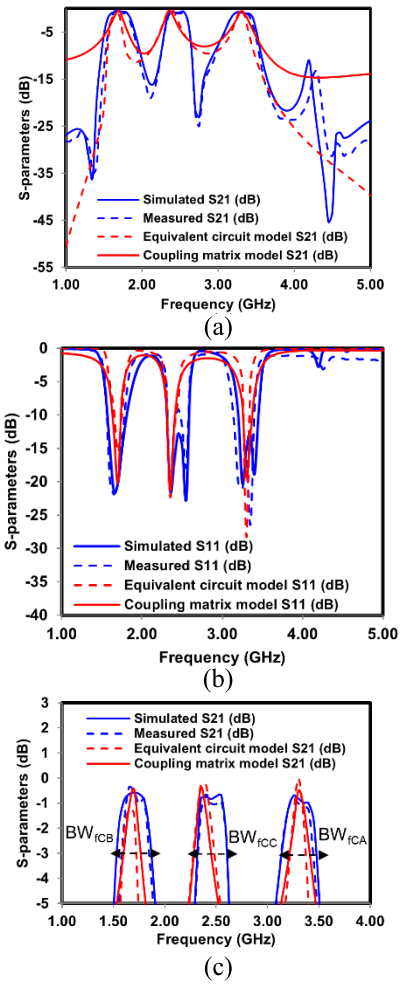

FIGURE 24. Simulated, measured, and equivalent circuit model results (a) $|S_{21}|$, (b) $|S_{11}|$, (c) bandwidth f_{CB}, f_{CC}, and f_{CA} at $|S_{21}| = -3$ dB.

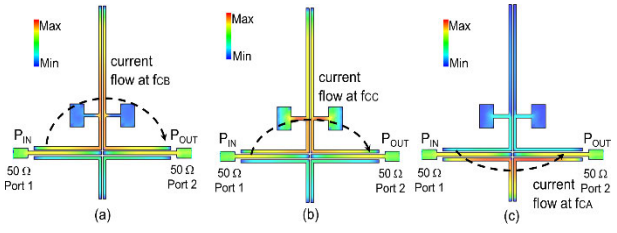

FIGURE 25. Surface current flow at (a) f_{CB}, (b) f_{CC}, and (c) f_{CA}.

TABLE 7. Comparison of multiband BPF results.

Parameters	f_{CB}		f_{CC}		f_{CA}	
	Sim	*Meas*	*Sim*	*Meas*	*Sim*	*Meas*
f_C *(GHz)*	1.70	1.65	2.55	2.55	3.25	3.25
FBW (%)	20.0	15.90	11.76	11.40	10.27	9.10
$\lvert S_{21} \rvert$ dB	-0.58	-0.39	-0.69	-0.92	-0.71	-0.80
$\lvert S_{11} \rvert$ dB	-21.6	-21.9	-22.6	-17.7	-20.2	-21.0
Isolation interband (ISO)	ISO_1 = -15.96 dB at 2.01 GHz (sim)				-	-
	ISO_1 = -19.05 dB at 2.01 GHz (meas)				-	-
	-	-	ISO_2 = -23.04 dB at 2.75 GHz (sim)			
	-	-	ISO_2 = -24.95 dB at 2.75 GHz (meas)			

*note: in our design $f_{CB} < f_{CC} < f_{CA}$, ISO_1 = isolation between f_{CB} and f_{CC}, ISO_2 = isolation between f_{CC} and f_{CA}

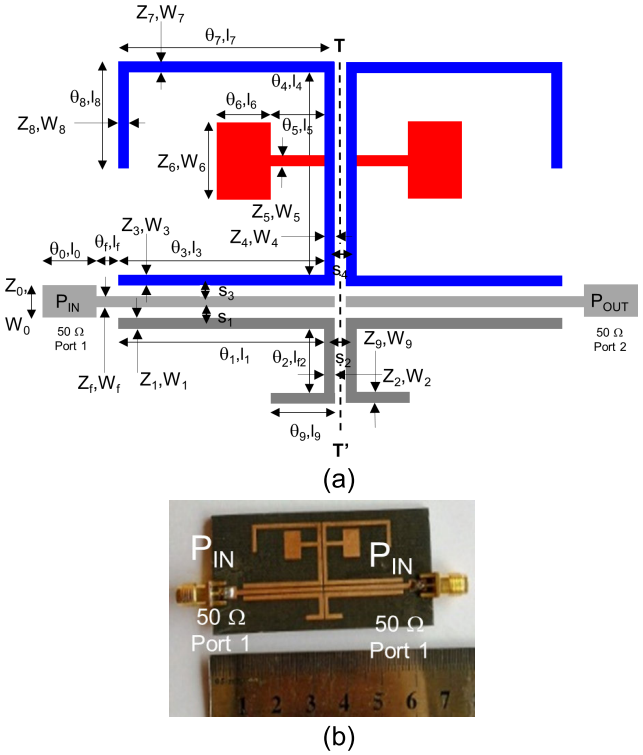

FIGURE 26. (a) The proposed miniaturized independent multiband BPF structure, (b) photograph of the fabricated miniaturized multiband BPF.

that the resonator is working independently and separately. The dual-band BPF design strategies are validated by good agreement between the measured and simulated results.

C. IMPLEMENTATION OF INDEPENDENT MULTIBAND BPF STRUCTURE

The parametric simulation results of the highly independent multiband BPF are shown in Fig 20(a) – 22(b). In our BPF design scenario, the value of the passbands are as follows: $f_{CA} > f_{CC} > f_{CB}$. The promising findings show that by varying the length (l_2), the passband f_{CA} can be tuned independently, as shown in Fig 20(a) and 20(b). By increasing the length (l_2), the passband f_{CA} will shift to a lower frequency. Varying the length (l_2) will not change the f_{CA} passband or the f_{CB} passband. This result demonstrates that the passband f_{CA} is more independent than the f_{CB} and f_{CC} passbands.

Fig 21(a) and 21(b) illustrate the $|S_{21}|$ characteristics with varied length (l_4) and the $|S_{11}|$ characteristics with varied length (l_4), respectively. There is a significant correlation between the length (l_4) and the f_{CB} passband. Fig 21(a) shows that by increasing the length (l_4), the f_{CB} passband will shift to a lower frequency. This change is not accompanied by a shift of the f_{CA} passband or the f_{CC} passband. Therefore,

TABLE 8. Coupling matrix of miniaturized independent multiband BPF.

M_{MN}	$M=S$	$M=1$	$M=2$	$M=3$	$M=4$	$M=5$	$M=6$	$M=7$	$M=8$	$M=L$
$N=S$	0	4.930	0	0	0	0	0	1.114	0	6.202
$N=1$	4.930	76.672	34.705	64.511	0	0	-1.954	0	0	0
$N=2$	0	34.705	0	59.158	0	0	0	0	0	0
$N=3$	0	64.511	59.158	0	0	0	0	0	0	0
$N=4$	0	0	0	0	0	-78.887	0.044	0	0	0
$N=5$	0	0	0	0	-78.887	0	8.937	0	0	0
$N=6$	0	-1.954	0	0	0.044	8.937	0.156	0	0	-2.522
$N=7$	1.114	0	0	0	0	0	0	0.001	0.273	0
$N=8$	0	0	0	0	0	0	0	0.273	0.001	-0.616
$N=L$	6.202	0	0	0	0	0	-2.522	0	-0.616	0

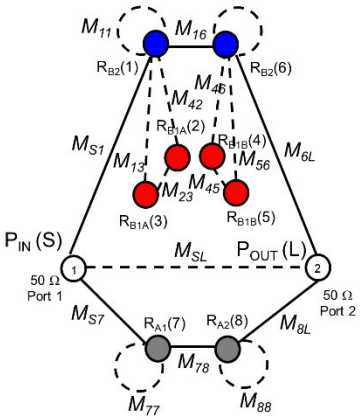

FIGURE 27. Coupling matrix.

TABLE 9. Dimensions of miniaturized multiband BPF.

N	W_N (mm)	l_N (mm)	s_N (mm)
f	1	2	-
0	3	5	-
1	1	23	0.5
2	1	6.5	0.5
3	1	23	0.5
4	1	15	0.5

N	W_N (mm)	l_N (mm)
5	1	5
6	7	4.75
7	1	20
8	1	7
9	1	5

TABLE 10. Comparison result of miniaturized multiband BPF.

Parameters	f_{CB}		f_{CC}		f_{CA}	
	Sim	*Meas*	*Sim*	*Meas*	*Sim*	*Meas*
f_C *(GHz)*	1.75	1.75	2.55	2.55	3.50	3.55
FBW (%)	22.84	21.20	5.49	4.70	8.37	8.40
$\lvert S_{21}\rvert$ dB	-0.61	-0.55	-0.95	-1.36	-0.92	-1.37
$\lvert S_{11}\rvert$ dB	-19.21	-18.2	-12.77	-21.29	-23.49	-22.3
Trans. zeros (Isolation interband)	ISO_1 = -26.60 dB at 2.35 GHz (sim)				-	-
	ISO_1 = -23.78 dB at 2.35 GHz (meas)				-	-
	-	-	ISO_2 = -31.55 dB at 2.80 GHz (sim)			
	-	-	ISO_2 = -30.61 dB at 2.80 GHz (meas)			

*note: for our design $f_{CB} < f_{CC} < f_{CA}$, ISO_1 = isolation between f_{CB} and f_{CC}, ISO_2 = isolation between f_{CC} and f_{CA}

the f_{CB} passband is more independent than the f_{CA} and f_{CC} passbands. The insertion loss values are better than -3 dB, and the reflection coefficient is lower than -10 dB.

Fig 22(a) and 22(b) illustrate the extraction of the $|S_{21}|$ and $|S_{11}|$ characteristics with varied length (l_6) and show that by varying the length (l_6), the values of $|S_{21}|$ and $|S_{11}|$ at the f_{CC} passband will shift. The f_{CC} passband will be shifted to a lower frequency by increasing the length (l_6) or to a higher frequency by decreasing the length (l_6). However, these changes have no effect on the f_{CA} passband or the f_{CB} passband. These results indicate that the f_{CC} passband is more independent than the f_{CA} and f_{CB} passbands. In summary, the passbands f_{CA}, f_{CB}, and f_{CC} are separately and independently influenced by length (l_2), length (l_4), and length (l_6), respectively. They are working with high independence. This important finding is proof that the designed multiband bandpass filter with a multicoupled line stub-SIR and a folding structure is highly independent.

Fig 23. (a) and 23(b) show the equivalent circuit model of the independent multiband BPF and a photograph of the fabricated multiband BPF, respectively. The dimensions of multiband BPF and the values of the equivalent circuit after optimization using the ADS software are shown in Table 6.

This multiband BPF structure also has a back-to-back resonator, so the coupling inter resonator is drawn as magnetic coupling. The third passband (f_{CC}) is generated by the SIR-structure, and the equivalent circuit model is clearly illustrated in Fig 23(a). Finally, the photograph of the fabricated multiband BPF with a 50-Ω port termination has a size of 0.32 $\lambda_G \times 0.31\ \lambda_G$, were λ_G is the wavelength of the fundamental frequency [34], [35] as shown in Fig 23(b).

After the multiband BPF has been fabricated, it should be tested by VNA for verification. Fig 24 (a), 24(b), and 24(c) show the simulated, measured, equivalent circuit model, and coupling matrix model results of $|S_{21}|$, $|S_{11}|$, $|S_{21}|$ for a bandwidth f_{CB} of -3 dB, and f_{CA} of -3 dB, respectively.

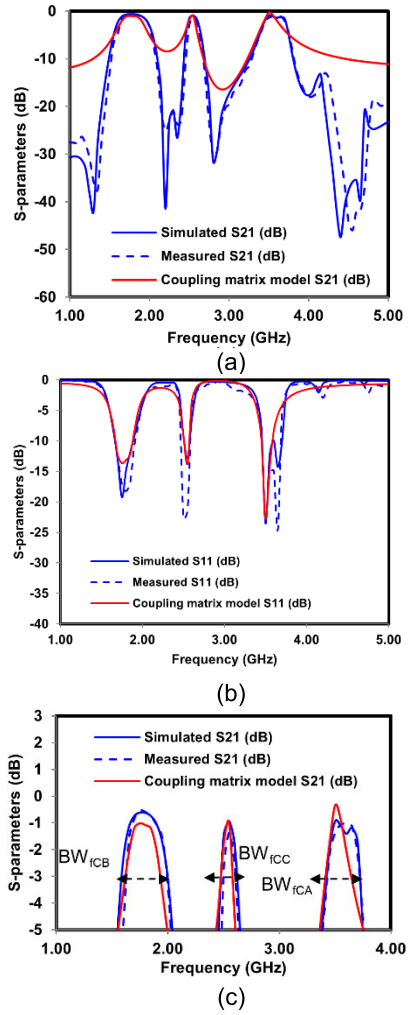

FIGURE 28. Simulated, measured, and equivalent circuit model results (a) $|S_{21}|$, (b) $|S_{11}|$, (c) bandwidth f_{CB}, f_{CC}, and f_{CA} at $|S_{21}| = -3$ dB.

Fig 25(a), 25(b) and 25(c) show the surface current flows at f_{CB}, f_{CC}, and f_{CA}, respectively. At the f_{CB} passband, the current distribution has flowed at the center resonator of R_B. The surface current distribution at the f_{CC} band has flowed at the SIR-structure. The f_{CA} band has flowed at the lower part of the feeding structure. This result indicates that the resonator is working independently and separately. The simulated and measured multiband BPF results are shown in Table 7.

D. MINIATURIZATION OF INDEPENDENT MULTIBAND BPF STRUCTURE

This section discusses the proposed miniaturization strategy. To reduce the multiband BPF size, a folded structure was proposed, as shown in Fig 26(a) and 26(b). Furthermore, Fig 27 shows the coupling matrix of miniaturized independent multiband BPF and the value of the coupling matrix is shown in Table 8. The value coupling matrix was obtained using optimization technique [12]. The nonlinear least-squares and the minimum-maximum algorithm were used.

TABLE 11. Performance comparison with other reported BPFs.

Ref	*Freq (GHz)*	$\lvert S_{21}\rvert$ (dB)	*-3 dB FBW (%)*	*Tz*	*Size* (λ_G^2)	*Independent passband* ($f_1/f_2/f_3$)	*Miniaturization*
[30]	1.95/ 3.46/ 5.25	-1.10/ -1.50/ -1.50	9.70/ 6.40/ 9.00	3	0.67	no/yes/no	no
[13]	1.57/ 2.40/ 3.45	-1.60/ -1.50/ -2.30	5.20/ 3.80/ 4.60	5	0.59	no/no/yes	no
[16]	1.80/ 3.50/ 5.20	-1.60/ -1.50/ -2.30	11.00/ 6.20/ 6.10	3	0.056	no/yes/no	no
[22]	2.40 / 3.50	-1.07 / -1.05	15.60/ 5.20	4	0.035	yes/yes	no
[23]	2.10 / 2.60	-0.68 / -1.08	2.15/ 1.48	3	0.028	yes/yes	no
[26]	1.57/ 3.50/ 5.80	-1.20/ -0.90/ -1.60	12.70/ 10.00/ 3.08	6	0.012	no/yes/yes	no
[27]	2.41/ 3.65/ 5.29	-1.91/ -1.42/ -1.51	6.20/ 12.2/ 11.8	5	0.012	yes/no/no	no
[28]	1.59/ 3.12/ 4.02	-1.11/ -1.12/ -1.11	15.70/ 12.70/ 5.71	5	0.033	no/yes/yes	no
Our Fig 23(b)	1.65/ 2.55/ 3.25	-0.39/ -0.92/ -0.80	15.90/ 11.40/ 9.10	5	0.099	yes/yes/yes	no
Our Fig 26(b)	1.75/ 2.55/ 3.55	-0.55/ -1.36/ -1.37	21.20/ 4.70/ 8.40	6	0.038	yes/yes/yes	yes

The dimensions of the compact multiband BPF after optimization using the ADS software are shown in Table 9.

The fabricated results are shown in Fig 26(b). After applying the folding structure, the multiband BPF size became 0.32 $\lambda_G \times 0.12\,\lambda_G$, where λ_G is the wavelength of the fundamental frequency. This method successfully reduced the multiband BPF dimensions by over 61.29 %. Fig 28 (a), 28(b), and 28(c) show the simulated, measured, and coupling matrix model results for $|S_{21}|$, $|S_{11}|$, $|S_{21}|$ for a bandwidth f_{CB}, f_{CC}, and f_{CA} of -3 dB, respectively. The results of the simulated and measured multiband BPFs are compared in Table 10.

Fig 29(a), 29(b) and 29(c) show the surface current flow at f_{CB}, f_{CC}, and f_{CA}, respectively. At the f_{CB} passband, the current distribution has flowed at the center resonator of R_B.

The surface current distribution at the f_{CC} band has flowed at the SIR-structure. The f_{CA} band has flowed at the lower part of the feeding structure. This result indicates that the resonator is working independently and separately. Finally, Table 11 illustrates the performance comparisons of some triple-band BPFs in terms of transmission zeros, isolation, size, and independent bands.

Based on these parameters, the proposed bandpass filter has the following advantages: 1) the multiband BPF has a highly independent inter passband, 2) the insertion loss $|S_{21}|$ (dB) value has excellent performance, 3) the isolation inter passband is good, 4) the proposed multiband BPF has a higher number of transmission zeros, 4) the proposed multiband BPF has a higher number of transmission zeros, 5) the filter has a compact size, and 6) the proposed BPF structure can be applied for 5G communication at 3.5 GHz. Furthermore, by using the folded structure, the multiband BPF has a

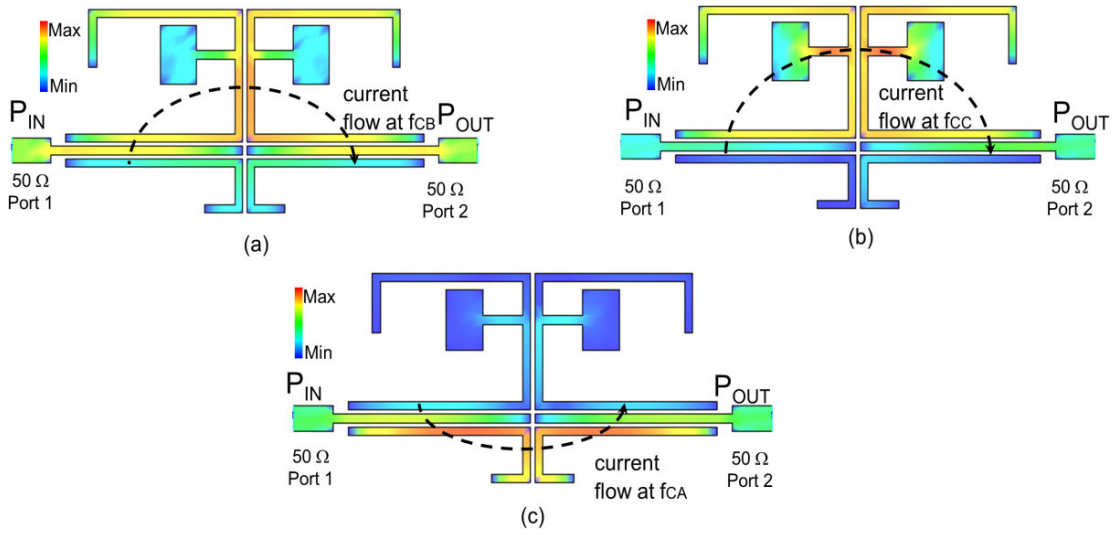

FIGURE 29. Surface current flow at (a) f_{CB}, (b) f_{CC}, and (c) f_{CA}.

compact size that is reduced by over 61.29 % compared to previous structures

IV. CONCLUSION

This paper describes the successful design and implementation of a highly independent and compact multiband BPF based on a multicoupled line stub-SIR with a folding structure. The multiband BPF is constructed with a multicoupled line to generate a highly independent inter passband. Moreover, the multiband performance is produced separately and independently by using three sets of resonators. To miniaturize the multiband BPF, a folding structure is also proposed. As a result, the proposed multiband BPF is very compact and reduces the size by over 61.29 %. This BPF is designed for applications such as GPS at 1.57 GHz, WCDMA (3G) at 1.8 GHz, WLAN (WiFi) at 2.4 GHz, LTE (4G) at 2.6 GHz, and 5G communication at 3.5 GHz. The simulated and measured results of the multiband BPF show good agreement. Finally, our proposed multiband BPF structure has a highly independent inter passband response and a compact size.

REFERENCES

[1] Y. Xie, F.-C. Chen, and Z. Li, "Design of dual-band bandpass filter with high isolation and wide stopband," *IEEE Access*, vol. 5, pp. 25602–25608, 2017, doi: 10.1109/ACCESS.2017.2773502.

[2] M. AbdulRehman and S. Khalid, "Design of tri-band bandpass filter using symmetrical open stub loaded step impedance resonator," *Electron. Lett.*, vol. 54, no. 19, pp. 1126–1128, Sep. 2018, doi: 10.1049/el.2018.5240.

[3] B. Liu and Y. Zhao, "COMPACT tri-band bandpass filter for WLAN and WIMAX using tri-section stepped-impedance resonators," *Prog. Electromagn. Res. Lett.*, vol. 45, pp. 39–44, Feb. 2014.

[4] B. Halvarsson, A. Simonsson, A. Elgcrona, R. Chana, P. Machado, and H. Asplund, "5G NR testbed 3.5 GHz coverage results," in *Proc. IEEE 87th Veh. Technol. Conf. (VTC Spring)*, Jun. 2018, pp. 1–5, doi: 10.1109/VTCSpring.2018.8417704.

[5] T. Firmansyah, S. Praptodinoyo, R. Wiryadinata, S. Suhendar, S. Wardoyo, A. Alimuddin, C. Chairunissa, M. Alaydrus, and G. Wibisono, "Dual-wideband band pass filter using folded cross-stub stepped impedance resonator," *Microw. Opt. Technol. Lett.*, vol. 59, no. 11, pp. 2929–2934, Nov. 2017, doi: 10.1002/mop.30848.

[6] T. Firmansyah, S. Praptodiyono, A. S. Pramudyo, C. Chairunissa, and M. Alaydrus, "Hepta-band bandpass filter based on folded cross-loaded stepped impedance resonator," *Electron. Lett.*, vol. 53, no. 16, pp. 1119–1121, Aug. 2017, doi: 10.1049/el.2017.1121.

[7] Q.-X. Chu, F.-C. Chen, Z.-H. Tu, and H. Wang, "A novel crossed resonator and its applications to bandpass filters," *IEEE Trans. Microw. Theory Techn.*, vol. 57, no. 7, pp. 1753–1759, Jul. 2009.

[8] F.-C. Chen and Q.-X. Chu, "Design of compact tri-band bandpass filters using assembled resonators," *IEEE Trans. Microw. Theory Techn.*, vol. 57, no. 1, pp. 165–171, Jan. 2009.

[9] V. K. Killamsetty and B. Mukherjee, "Miniaturised highly selective bandpass filter with very wide stopband using meander coupled lines," *Electron. Lett.*, vol. 53, no. 13, pp. 889–890, Jun. 2017, doi: 10.1049/el.2017.1270.

[10] J. Xu, H. Wan, J. Ding, and Y. Zhu, "Miniaturised tri-band lowpass–bandpass filter using lumped-element structure," *Electron. Lett.*, vol. 55, no. 5, pp. 272–274, 2019, doi: 10.1049/el.2018.8054.

[11] X. Guo, L. Zhu, and W. Wu, "Design method for multiband filters with compact configuration in substrate integrated waveguide," *IEEE Trans. Microw. Theory Techn.*, vol. 66, no. 6, pp. 3011–3018, Jun. 2018, doi: 10.1109/TMTT.2018.2830337.

[12] K. Zhou, C.-X. Zhou, H.-W. Xie, and W. Wu, "Synthesis design of SIW multiband bandpass filters based on dual-mode resonances and split-type Dual- and triple-band responses," *IEEE Trans. Microw. Theory Techn.*, vol. 67, no. 1, pp. 151–161, Jan. 2019, doi: 10.1109/TMTT.2018.2874250.

[13] T. Unno and N. Sekiya, "Compact high-pole HTS triband bandpass filters using a new feeding structure," *IEEE Trans. Appl. Supercond.*, vol. 28, no. 4, Jun. 2018, Art. no. 1500305, doi: 10.1109/TASC.2018.2797980.

[14] W.-Y. Chen, M.-H. Weng, and S.-J. Chang, "A new tri-band bandpass filter based on stub-loaded step-impedance resonator," *IEEE Microw. Wireless Compon. Lett.*, vol. 22, no. 4, pp. 179–181, Apr. 2012, doi: 10.1109/LMWC.2012.2187884.

[15] J. Xu, W. Wu, S. Member, and C. Miao, "Compact microstrip dual-/tri-/quad-band bandpass filter using open stubs loaded shorted stepped-impedance resonator," *IEEE Trans. Microw. Theory Techn.*, vol. 61, no. 9, pp. 3187–3199, Sep. 2013, doi: 10.1109/TMTT.2013.2273759.

[16] C.-H. Lee, C.-I.-G. Hsu, and H.-K. Jhuang, "Design of a new tri-band microstrip BPF using combined quarter-wavelength SIRs," *IEEE Microw. Wireless Compon. Lett.*, vol. 16, no. 11, pp. 594–596, Nov. 2006.

[17] W. Y. Chen, Y. H. Su, H. Kuan, S.-J. Chang, "Simple method to design a tri-band bandpass filter using asymmetric SIRs for GSM, WIMAX, and WLAN applications," *Microw. Opt. Technol. Lett.*, vol. 53, no. 7, pp. 1573–1576, 2011, doi: 10.1002/mop.26037.
[18] W. Y. Chen, M. H. Weng, S. J. Chang, H. Kuan, and Y.-H. Su, "A new tri-band bandpass filter for GSM, WiMAX and ultra-wideband responses by using asymmetric stepped impedance resonators," *Prog. Electromagn. Res.*, vol. 124, pp. 365–381, Feb. 2012.
[19] Y. Mo, K. Song, and Y. Fan, "Miniaturized triple-band bandpass filter using coupled lines and grounded stepped impedance resonators," *IEEE Microw. Wireless Compon. Lett.*, vol. 24, no. 5, pp. 333–335, May 2014, doi: 10.1109/LMWC.2014.2310458.
[20] H.-W. Liu, Y. Wang, X.-M. Wang, J.-H. Lei, W.-Y. Xu, Y.-L. Zhao, B.-P. Ren, and X.-H. Guan, "Compact and high selectivity tri-band bandpass filter using multimode stepped-impedance resonator," *IEEE Microw. Wireless Compon. Lett.*, vol. 23, no. 10, pp. 536–538, Oct. 2013, doi: 10.1109/LMWC.2013.2251618.
[21] Q. Chu and X. Lin, "Advanced triple-band bandpass filter using tri-section SIR," *Electron. Lett.*, vol. 44, no. 4, pp. 295–296, 2008, doi: 10.1049/el:20083096.
[22] D. Li, Y. Zhang, X. Feng, K. Song, and Y. Fan, "Dual-band bandpass filter with controllable center frequency and bandwidth using short stub-loaded SIR and tri-section SIR," *AEU - Int. J. Electron. Commun.*, vol. 69, no. 7, pp. 1004–1009, Jul. 2015, doi: 10.1016/j.aeue.2015.03.004.
[23] A. Ghaderi, A. Golestanifar, and F. Shama, "Design of a compact microstrip tunable dual-band bandpass filter," *AEU-Int. J. Electron. Commun.*, vol. 82, pp. 391–396, Dec. 2017, doi: 10.1016/j.aeue.2017.10.002.
[24] B. Pal and S. Dwari, "Microstrip dual-band bandpass filter with independently tunable passbands using varactor-tuned stub loaded resonators," *AEU - Int. J. Electron. Commun.*, vol. 73, pp. 105–109, Mar. 2017, doi: 10.1016/j.aeue.2017.01.004.
[25] J.-K. Xiao, Y. Li, X.-W. Li, Y.-F. Zhu, and J.-G. Ma, "Controllable miniature tri-band bandpass filter using defected microstrip structure," *Electron. Lett.*, vol. 50, no. 21, pp. 1534–1536, Oct. 2014, doi: 10.1049/el.2014.1432.
[26] D. Lu, N. S. Barker, and X. H. Tang, "Compact and independently-design tri-band bandpass filter with bandwidth and return loss control," *Electron. Lett.*, vol. 52, no. 24, pp. 1992–1994, Nov. 2016, doi: 10.1049/el.2016.3247.
[27] Q.-X. Chu, X.-H. Wu, and F.-C. Chen, "Novel compact tri-band bandpass filter with controllable bandwidths," *IEEE Microw. Wireless Compon. Lett.*, vol. 21, no. 12, pp. 655–657, Dec. 2011, doi: 10.1109/LMWC.2011.2172593.
[28] N. Kumar and Y. K. Singh, "Compact tri-band bandpass filter using three stub-loaded open-loop resonator with wide stopband and improved bandwidth response," *Electron. Lett.*, vol. 50, no. 25, pp. 1950–1952, Dec. 2014, doi: 10.1049/el.2014.3425.
[29] G. Shen, W. Che, and Q. Xue, "Novel tri-band bandpass filter with independently controllable frequencies, bandwidths, and return losses," *IEEE Microw. Wireless Compon. Lett.*, vol. 27, no. 6, pp. 560–562, Jun. 2017, doi: 10.1109/LMWC.2017.2701302.
[30] F. Wei, P.-Y. Qin, Y. J. Guo, C. Ding, X. W. Shi, "Compact balanced dual-and tri-band BPFs based on coupled complementary split-ring resonators (C-CSRR)," *IEEE Microw. Wireless Compon. Lett.*, vol. 26, no. 2, pp. 107–109, Feb. 2016, doi: 10.1109/LMWC.2016.2517125.
[31] C. H. Kim and K. Chang, "Independently controllable dual-band bandpass filters using asymmetric stepped-impedance resonators," *IEEE Trans. Microw. Theory Techn.*, vol. 59, no. 12, pp. 3037–3047, Dec. 2011, doi: 10.1109/TMTT.2011.2168973.
[32] J. S. Hong and M. J. Lancaster, *Microstrip Filters for RF/Microwave Applications*. New York, NY, USA: Wiley, 2001.
[33] J. K. Xiao, Y. Li, M. Zhu, W. Zhao, L. Tian, and W. J. Zhu, "High selective bandpass filter with mixed electromagnetic coupling and source–load coupling," *AEU-Int. J. Electron. Commun.*, vol. 69, no. 4, pp. 753–758, Apr. 2015, doi: 10.1016/j.aeue.2015.01.007.
[34] Y. Feng, B. Wei, Z. Xu, F. Song, B. Cao, X. Guo, X. Lu, and X. Zhang, "Tri-band superconducting bandpass filter with controllable passband specifications," *Electron. Lett.*, vol. 50, no. 20, pp. 1456–1457, Sep. 2014, doi: 10.1049/el.2014.2352.
[35] L. Gao, X. Y. Zhang, B.-J. Hu, and Q. Xue, "Novel multi-stub loaded resonators and their applications to various bandpass filters," *IEEE Trans. Microw. Theory Techn.*, vol. 62, no. 5, pp. 1162–1172, May 2014, doi: 10.1109/TMTT.2014.2314680.

TEGUH FIRMANSYAH (Member, IEEE) was born in Subang, Indonesia. He received the B.Eng. (S.T.) degree in electrical engineering and the M.Eng. (M.T.) degree in telecommunication engineering from the Department of Electrical Engineering, Universitas Indonesia, in 2010 and 2012, respectively, where he is currently pursuing the Ph.D. degree in electrical engineering. In 2012, he joined the Department of Electrical Engineering, Universitas Sultan Ageng Tirtayasa, as a Researcher and a Lecturer. He has authored or coauthored over 25 articles published in refereed journals and conferences. He holds two patents for wideband antenna and multiband antenna. His research interests include microstrip antenna and microwave circuit for various applications. He is a member of the IEEE Antenna and Propagation Society (AP-S) and the IEEE Microwave Theory and Technique Society (MTT-S). He has been a Reviewer for *Electronics Letters* (IET), the *International Journal of Microwave and Wireless Technologies* (Cambridge), *Wireless Personal Communications* (Springer), the *International Journal of Electronics and Communications* (Elsevier), *Microwave and Optical Technology Letters* (Wiley), the *International Journal of RF and Microwave Computer-Aided Engineering* (Wiley), and IEEE Access.

MUDRIK ALAYDRUS (Senior Member, IEEE) received the Dipl.Ing. degree in electrical engineering from Leibniz Universität Hannover, in 1997, and the Dr. Ing. degree in electrical engineering from the University of Wuppertal, in 2001. Since 2003, he has been working at Universitas Mercu Buana, Jakarta. He has authored more than 100 publications, including three text books: Electromagnetics, Transmission Lines, and Antennas. He holds a granted patent and two patent pendings. In 2006, he founded the Laboratory Advanced Telecommunication and Applied Electromagnetics in the Department of Electrical Engineering at Universitas Mercu Buana. His current research interests include microwave and millimeter wave components, wireless power transfers, wireless sensor networks, interaction between electromagnetics and materials, and mathematical modeling in signal processing. He is a member of Verein Deutschen Elektroingenieure (VDE). He is a Reviewer of several reputable journals, including the IEEE Transactions on Antennas and Propagation.

YUYU WAHYU (Member, IEEE) was born in Bandung, Indonesia, in February 1962. He received the Ir. (Insinyur) degree, the M.Eng. (M.T.) degree in telecommunication information system from electrical engineering study program, and the Ph.D. degree in global information and telecommunication studies from the School of Electrical and Informatics Engineering, Institut Teknologi Bandung, Bandung, Indonesia, in 1990, 2000, and 2010, respectively.

He has been with the Telecommunications Research Center, Strategic Electronics, Components and Materials (Telkoma) Indonesian Institute of Sciences (LIPI) (now the Research Center for Electronics and Telecommunications, LIPI), since 1991. He was the Head of the Telecommunications and Radio Laboratory, from 2000 to 2003, and research facilities, from 2010 to 2016. He has been the Chair of the Research Group of Antennas and Propagation, since 2014. Since 2019, he has been appointed as a Research Professor in telecommunications transmission. He followed a number of activities related to his field of competence, including Guest Research in Okayama, Japan, in 2003, for 1.5 months on the topic of Active Antenna and Radar Training, in 2006 and 2007, at IRCTR-TU, Delft, The Netherlands. He conducted FMCW radar research from 2006 to present and electronic support measure (ESM), from 2015 to 2018. He participated in professional organizations, including: Himpenindo (Association of Indonesian Researchers), since 2018, the Indonesian Radar Association, since 2008, and the IEEE Antenna and Propagation Society, since 2010.

EKO TJIPTO RAHARDJO (Member, IEEE) was born in Pati, Indonesia, in April 1958. He received the Ir. (Insinyur) degree from Universitas Indonesia, Jakarta, Indonesia, in 1981, the M.S. degree from the University of Hawaii at Mānoa, Honolulu, HI, USA, in 1987, and the Ph.D. degree from Saitama University, Urawa, Japan, in 1996, all in electrical engineering.

He has been a Teaching Assistant with the Department of Electrical Engineering, Universitas Indonesia, since 1982. Since 2005, he has also been appointed as a Professor in electrical engineering. He was the Chairman of University Senate of Universitas Indonesia, from 2011 to 2012. He was the Head of Electrical Engineering Department, Universitas Indonesia, from 2004 to 2008. He was the Executive Director of the Quality Undergraduate Education (QUE) in the Department of Electrical Engineering, Universitas Indonesia, from 1999 to 2004, where he was also the Head of Telecommunication Laboratory, from 1997 to 2004. Since 2003, he has been the Director of Antenna Propagation and Microwave Research Group (AMRG), Universitas Indonesia. His research interests include antenna engineering, wave propagation, microwave circuits and communication systems, and telecommunication system regulations. He has been published and presented more than a 100 research articles both national and international journals and symposiums.

Dr. Rahardjo is a member of the IEEE Antenna and Propagation Society (AP-S) and the IEEE Microwave Theory and Technique Society (MTT-S). He has also been a member of the International Steering Committee (ISC) of Asia Pacific Microwave Conference (APMC), since 2010, and the International Advisory Board of International Symposium on Antenna and Propagation (ISAP), since 2012. He was a recipient of the Indonesian Government Scholarship through MUCIA, from 1984 to 1987, the Hitachi Scholarship, from 1992 to 1996, the Young Researcher's Award from Universitas Indonesia, in 1996, the Second Winner of Best Researcher Award in Science and Technology Universitas Indonesia, in 2009, and the Second Winner of Best Teaching Award Universitas Indonesia, in 2010. He was the Founder of the IEEE Joint Chapter MTT-S/AP-S Indonesia. He has served as the President of IEEE Joint Chapter MTT-S/AP-S, IEEE Indonesia Section, from 2009 to 2010 and from 2014 to 2015. He is the General Chairman of the Indonesia Malaysia Microwave and Antenna Conference (IMMAC) 2010 held in Jakarta, and the Indonesia Japan Joint Scientific Symposium (IJJSS) 2010 held in Bali, and the General Co-Chairman of the Indonesia Japan Joint Scientific Symposium (IJJSS) 2012 held in Chiba, Japan.

GUNAWAN WIBISONO (Member, IEEE) received the B.Eng. degree in electrical engineering from the University of Indonesia, Depok, Indonesia, in 1990, and the M.Eng. and Ph.D. degrees from Keio University, Japan, in 1995 and 1998, respectively. He is a former Head of the Electrical Engineering Department, University of Indonesia. His research interests include coding and wireless communications, electronics and optical communications, and telecommunication regulation.